

Microstructural changes due to fatigue of $Al_{0.1}CoCrFeNi$ high entropy alloys studied by electron backscatter diffraction: EBSD scanning of large areas

Sebastiaan van Baars

Prof. Jeff de Hosson

Dr. Vaclav Ocelik

Dr. Indrinil Basu

March 26, 2018

Abstract

In this research, electron backscatter diffraction is used in order to analyse the microstructural properties of $Al_{0.1}CoCrFeNi$ high entropy alloys subjected to different cyclic loading tests as well as different heat treatments. In order to obtain maps with microstructural information regarding the samples, 2 different methods are used in order to scan large areas of the sample surface:

1. merging method: this method involves merging various data maps of small scans at high magnification together.
2. large scan method: this method involves making large scans of areas at a much lower magnification.

The merging method has been attempted but did not lead to successful outcomes of the microstructural maps of the materials due to various different distortions present which become problematic when attempting to merge data maps. The distortions have been quantified in order to understand how one can disqualify them from influencing EBSD data maps and to allow for merging. From this analysis it is concluded that merging methods require very high magnifications to be successful and are thus not of use for this research.

The microstructural characteristics of the materials are analysed using the large scan method which proves less problematic. Finally, an analysis is made with regards to how various different mechanical properties relate to the microstructural characteristics of the materials investigated with an emphasis on the internal strain distributions. This analysis is generally a success however, remains a matter of statistics since most conclusions are derived from visual analysis of the maps.

Contents

1	Introduction	3
2	A brief overview of fatigue and crack initiation	4
3	Methods and materials	5
3.1	Working principles of SEM	5
3.2	Working principles of EBSD	7
3.3	Merging of EBSD data sets	11
3.4	Selected settings and experimental methods for scanning	12
3.5	Samples analysed	16
4	Method 1: merging of data sets	17
4.1	Scanning method and results	17
4.2	Discussion and methods for improvement	18
4.3	Quantifying EBSD distortions	19
4.4	Final discussion for merging methods	22
5	Method 2: Large scans	24
5.1	Analysis of OIM measurements	24
5.1.1	Data cleaning process	24
5.1.2	Map types	25
5.2	EBSD maps and results	26
5.2.1	Non-fractured, as cast, 979N, fatigue affected area	27
5.2.2	Non-fractured, as cast, 979N, non-fatigue affected area	29
5.2.3	Non-fractured, 400h at 700°C 2780 N, fatigue affected area	31
5.2.4	Non-fractured, 400h at 700°C 2780 N, non-fatigue affected area	33
5.2.5	Fractured, as cast, 3114N	35
5.2.6	Fractured, 400h at 700°C 3114N	37
5.2.7	Fractured, as cast, 3336 N	39
5.2.8	Fractured, 400h at 700°C 3336N	41
5.2.9	Effects observed throughout all samples	42
5.2.10	Fractured vs non-fractured	43
5.2.11	Temperature treatments	44
5.2.12	Cyclic load applied	45
5.3	Discussion	45
6	Conclusion	46
7	Appendices	48
8	References	49

1 Introduction

High entropy alloys (HEA's) are currently a subject with high attention in the materials science community. Having only been well established in scientific publications since 2004, they have already grown into a rapidly evolving field due to the vast number of new materials within its design space and the unexplained and complex properties that these materials carry.

Although HEA's materials are not yet certified for application, very innovative and exceptional properties have already been found which are promising for applications such as coatings for wear resistance, diffusion barriers, structural as well as high temperature properties, which may be of interest for fusion technology advancements.

Unlike conventional alloys which are designed to have a single major element, HEA's consist of near equal ratios of 5 or more elements which crystallise as a single phase, the result of which 4 distinctive new physical effects come to play[5]:

1. high configurational entropy
2. strained lattices
3. sluggish diffusion kinetics
4. and the so called "cocktail effect"

By now, each of these effects have become distinctive research subbranches within HEA's research and serve as guidelines for further research. In this paper, attention is shifted to the mechanical properties of these materials with an emphasis on the strain distributions due to fatigue.

In general, fatigue is defined as the strain response of a material to cyclic loading, where a single cycle does not produce cracks/deformations, whereas a vast number of such cycles leads to the eventual failure of the material.

Mechanical structures which suffer from such effects during use can be found all around us, from aircraft wings due to aeroelastic effects, to factory machines and propulsion systems for their non-stop continual identical motion. The failure of structures due to such effects constitutes approximately 4% of the gross domestic product of the US alone[1]. This causes microstructural knowledge of the physics of fatigue and the search for new materials such as HEA's with possible future prospects for improved cyclic loading properties, to be of great importance in the materials science and engineering in order to lead improvement in the community.

Various studies have already been published regarding the mechanical properties of cyclically loaded HEA's failure[7], however, when it comes to a microstructural analysis, the literature is limited.

In this paper, the microstructural properties of HEA's are researched with electron backscatter diffraction (EBSD). EBSD is an advanced microscopy tool

which is an extension of Scanning electron microscopy (SEM), and can be used in order to derive a wealth of information regarding microstructural changes due to fatigue, which can then be quantified accurately with advanced software tools.

The main technology of both systems is the use of an electron beam in high vacuum in order to collect information regarding the sample topography, however, while SEM technology simply collects the number of electrons which are emitted from the sample surface, EBSD technology uses a phosphorous screen in order to analyse the pattern of the scattered electrons, allowing for a much more detailed analysis of the sample surface.

The goal of this research is to use EBSD in order to examine the microstructural effects of fatigued areas of various $Al_{0.1}CoCrFeNi$ high entropy alloy samples, which were subjected to different fatigue conditions, as well as different heat treatments.

In order to encapsulate as many grains as possible of the fatigued area, very big scanning areas are required which will be examined through 2 main methods:

1. performing EBSD scans at high magnifications and merging the acquired data sets together using the appropriate software. Such method could potentially yield more information regarding the microstructural properties as the technology used is very capable making high magnification scans with high details. This method is however, experimental itself since it has not been performed notably before.
2. performing EBSD scans at a lower magnification and selecting big scan areas. This method is well established and can be used if problems are encountered with regards to the first method, however, it won't be able to encapsulate as many details.

2 A brief overview of fatigue and crack initiation

Cyclic loading of a material causes dislocation motion through 2 processes: slip and twinning. In polycrystalline alloys the slip is prevalent over twinning and its motion is activated when the critical resolved shear stress is reached in a preferentially oriented grain. Once this occurs, the dislocations can glide throughout the slip system until obstructions are encountered such as precipitates, another dislocation motion, a solute particle or a grain boundary. When the obstacle is reached, further cyclic loading may cause the dislocation motion to overcome the obstacle by processes such as shear, climbing, cross-slip, etc... Regardless of which mechanism occurs, the path followed by the dislocation motion is the path of least energy which will also be followed by subsequent dislocation motions. As the dislocations drift towards the same low energy point, a dislocation band is formed called: "persistent slip band".

Due to forward and reverse loading, opposing dislocations are also created, which propagate in similar fashion in order to minimise the total energy of the system. If positive and negative dislocation climb or cross slip with one another

they are annihilated leading to vacancies in the lattice.

When the density of dislocations in a persistent slip band increases along with the magnitude of dislocation interactions, the slip band can exhibit work hardening behaviour. At the same time, diffusion of vacancies towards grain boundaries and free surfaces can produce material ex/intrusions or ledges.

The result of a vast number of dislocations piling up at a grain boundary can result in a large concentration of stress, which can eventually lead to the activation of slip dislocations motions in the surrounding grains. most of the strain is localised within a small region of the persistent slip band.

Finally, patterns of dislocations will cause some areas within the slip band to be harder than others leading to crack initiation at the interface of the hard and soft areas of the slip band. Thus cracks are created and material failure is initiated.

3 Methods and materials

3.1 Working principles of SEM

The SEM system used(XL310 ESEM-FEG from Philips), consists of the following components which are arranged as presented in figure 1:

1. An **electron source** located above an **anode** pointing vertically downwards used to accelerate the electron beam. The electrons in this beam are defined as primary electrons.
2. an electromagnetic **condenser lens** used to direct the beam to the next stage.
3. A series of coils connected to analogue to digital(A/D) converter(**deflection joke**). This system was used to alter the trajectory of the beam to the required scanning points on the material surface to produce a raster scan.
4. A (**detector**) which consists two positively biased grids and two photomultipliers.

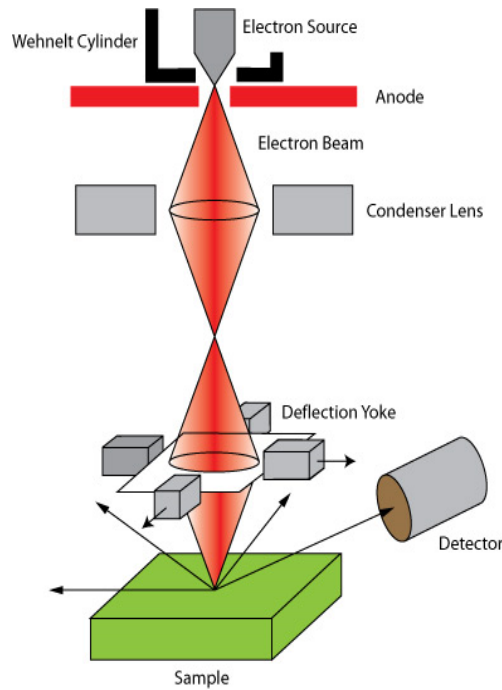


Figure 1: recreation of the components of the SEM model XL310 ESEM-feg from Philips. Note that in this figure, a single condenser lens is presented for the purpose of describing the system. A complete recreation of the system involves 2 condenser lenses

When the electron beam impacts the material surface, various interactions could occur at the atomic level:

1. the electron is absorbed
2. a molecule on the analysed material is excited and subsequently emits another electron (inelastic scattering). These electrons are defined as secondary electrons.
3. the electron is elastically reflected

Out of all the above mentioned interactions, secondary electrons have the least energy ($\approx 50\text{eV}$). This causes the positively biased grid attraction to absorb them into the detector. After the initial absorption by the detector they are accelerated by a second grid at high voltage towards the scintillator-photomultiplier which produces catholuminescence flashes and are conducted to a second photomultiplier in order to convert them to an electrical signal. This signal is finally used to reconstruct topographical surface information with microscopy software. All measurements taken in the described configuration are taken in a high vacuum chamber.

3.2 Working principles of EBSD

Collection of diffraction patterns

As mentioned before, EBSD uses a phosphorus screen in order to analyse the pattern of scattered electrons. Such patterns are called Kikuchi bands and are to be collected at each point of the raster scan. To begin with, the sample is tilted to an angle of $70 - 75^\circ$. The specific reason for this angle, can be traced to two key variables each of which linearly oppose one another when it comes to obtaining optimal diffraction patterns:

1. The ratio of intensity at the edge of the pattern compared to the ratio at the centre of the pattern. Such a curve would show optimal image data for long specimen to screen distances
2. Intensity as a function of distance to the phosphor screen. Such a curve, logically represents optimal data for short specimen to screen distance

When both curves are plotted on a single diagram, they will meet at a point where the tilting angle is in the range of $70 - 75^\circ$.

Once successfully tilted, the EBSD measuring sensor, which consists of a phosphor screen is moved into place into the high vacuum chamber using an automated motion control system which places the screen to an adequate distance from the tilted sample for data collection.

At this stage, the electron beam source can be used with identical operation methods as when used for SEM data collection. Now however, the phosphor screen is used for data collection as presented in Figure 2[4].

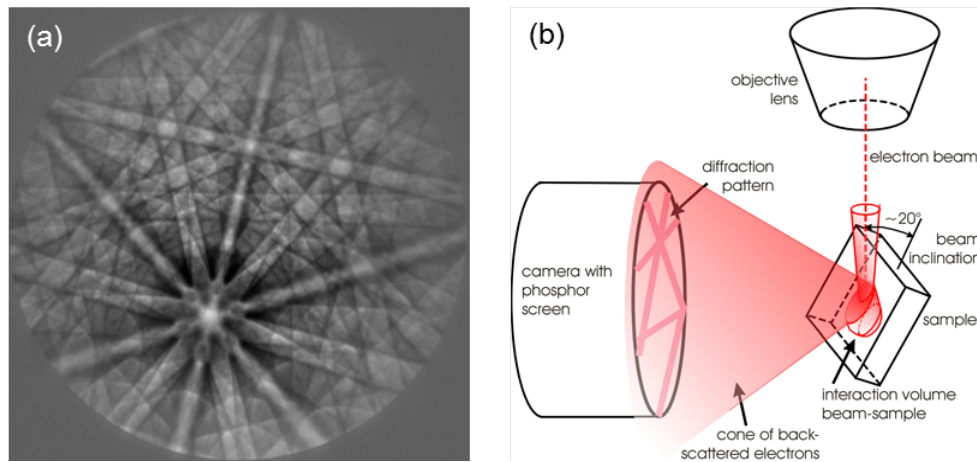


Figure 2: Figure 2b presents the tilted sample and the diffraction pattern of the electron beam to the phosphor screen. figure 2a presents the captured Kikuchi pattern at that specific point of the raster scan.

Automatic analysis method of Kikuchi patterns through Hough transforms

Once a Kikuchi pattern is captured, a Hough transform is required in order to realize automatic crystal orientation calculation.

Such transforms examine individual points on a Kikuchi band edge and relates them to the infinite amount of lines such a point could be part of. This is done by transforming a point on a Kikuchi band edge defined by (x, y) coordinates into a sequence of points of a sinusoidal curve in Hough space (See figure 3[3] (Note that for the matter of presenting the algorithm, a binary image line is used instead of a Kikuchi band image))

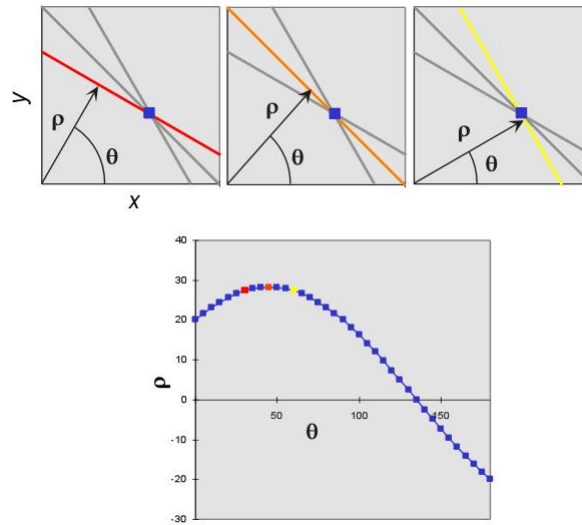


Figure 3: The figure presents how a single coordinate can be transformed into 3 (red, orange and yellow) line segments defined by coordinates ρ , θ in Hough space. The point can be defined by a sequence of other lines segments which are not highlighted in Hough space.

In order for Hough space to carry significant information, such an algorithm is to be ran with various points on a Kikuchi band edge (see figure 4[3])

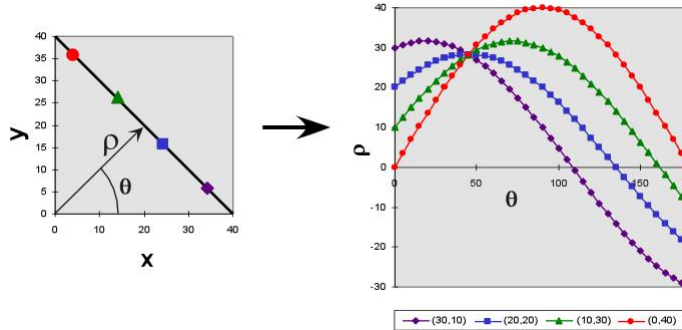


Figure 4: Hough transform of 4 points (red, green, blue, purple) on a Kikuchi band image space and its subsequent transformation into Hough space. At this point in Hough space, a single point is observed where all sinusoidal curves intersect. These points coincide with the ρ and θ values which correspond with the line segment of the Kikuchi band observed in the (x, y) space

Broadly speaking, this numerical method allows for the computer to identify where band lines are on Electron backscatter patterns (EBSP's) and what their directions are, making it a requirement for the final stage.

automatic indexing of EBSP's

Once Hough transforms are evaluated for a single EBSP of the raster scan, the data needs to be matched computationally with the phase data which has been pre-selected for the researched material type. In this research the pre-selected settings are "fcc generic HEA" and "bcc generic HEA" phases. The key idea here is that the Kikuchi band data is used in combination with theoretical material information in order to quantify the experimental image data. The matching process can be briefly summed up as follows:

1. The (hkl) values of the bands most likely to be detected by the Kikuchi bands are selected. All equivalent (hkl) values are also determined since the specific material orientations at a point are unknown. These sets of bands are paired with one another and their angles are calculated. Once all the possible angles are calculated the duplicate angles are removed.
2. Using the derived combinations of (hkl) values and their angles, the matching process can be performed with the Kikuchi bands. In order to take into consideration not only the angles, but also the width of the bands, 3 (hkl) values are used to match with a single triangle from the Kikuchi band data.

The graphical result of the process are presented in Figure 6.

Since each band consists of a straight line which intersects various triangles in the EBSP instead of a single triangle, a single matched triangle must also contain the correct information for the matching of other triangles which use the same (hkl) 's. For an arbitrary number of bands n , the number of triplets

which need to be matched as accurately as possible can be calculated as follows:

$$\text{triplet number} = \frac{n!}{(n-3)!3!}$$

In order to optimise the accuracy of the data. A logical step would require as many triplets to be indexed as solutions based on the EBSD settings. This however, is a imprecise statement since the number of indexed solutions does not validate the accuracy of the matched data. For this reason, a measure of accuracy is calculated known as the Confidence index(CI)

The confidence index, uses both the highest voted(V_1) and second highest voted(V_2) indexing solutions in order to obtain an accuracy measure for the matched data:

$$CI = \frac{V_1 - V_2}{V_1}$$

From a theoretical standpoint, CI values are directly related to the fraction of correctly indexed patterns(see figure5)[2]:



Figure 5: Theoretical relation between confidence index and fraction of correctly indexed patterns

A second parameter used to quantify the quality of the indexed pattern is the fit quality. Fit quality makes use of the geometry of the difference between the Hough transform derived bands as well as the indexed patterns. This parameter sums up the angular deviations of each indexed pattern as compared to the transform derived bands and sums the values together.

All band indexing methods are performed computationally and the only concern of this research is the Confidence index(CI), the fit quality which represent the accuracy of data collection, and of course, the Euler angles which specify what was measured at that point.

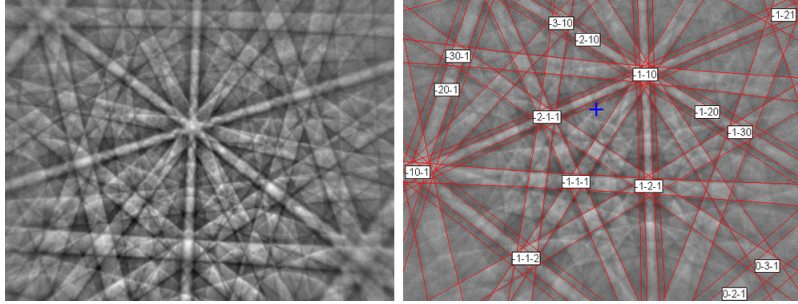


Figure 6: The left image represents a typical Kikuchi pattern and the right figure presents the same Kikuchi pattern, indexed with various (hkl) values.

EBSD map formation and limitations to the stepsize

As mentioned before Euler angles are used in order to quantify the orientation of the crystal at a specific point. This process is repeated throughout the entire sampling area in order to construct 2D images which contain the orientation properties of individual points, where each point has its own CI and IQ value. When zoomed in to the maximum, each data point on the map is presented as a hexagonal geometric shape such that the distance between every point, and their neighbours in any direction, is the same throughout the entire scan. The maximum amount of 1 dimensional steps the microscope is capable of making in order to produce hexagonal data points which do not overlap with one another, is a function of the step size of the electronic A/D converter which is ≈ 1000 steps in one dimension. This can be used to find the minimal step size at a specific magnification:

$$minimum\ step\ size = \frac{field\ of\ view}{1000}$$

Finally, it must be taken into account that the maximal resolution at which realistic EBSD data collection can be performed is $50nm$ [8]

3.3 Merging of EBSD data sets

EBSD microscopy methods suffer from distortions which change the geometry of a scanning area and its subsequent data map. In order to appropriately merge EBSD data sets, 2 key distortions must be minimised such that geometrical deviations of the merged data samples become negligible:

1. trapezoidal distortions
2. the so called "fish eye effect" distortions

The trapezoidal distortions are primarily present due to the tilting of the sample surface, an unavoidable experimental error factor when using current EBSD technology as a whole. Such distortions are caused by deviations of the

beam trajectory at the far end of the sample, as compared to the upper end(see Figure7)

The trapezoidal distortion effect can be quantified simply by measuring the percentage difference in lengths between the upper and lower sides:

$$\text{trapezoidal distortion percentage} = \left(\frac{x_T - x_B}{x_T} \right) \times 100 \quad (1)$$

However, various other geometric lengths presented in the figure can also be used to measure other distortions if necessary.

The fish eye effect, is presented in figure 8. In order to measure the fish eye effect, a similar equation can be applied as for the trapezoidal distortion:

$$\text{FE distortion percentage} = \left(\frac{L_m - L_R}{L_m} \right) \times 100 \quad (2)$$

In order, to minimise both distortions types, their magnitude at different magnifications is to be analysed.

3.4 Selected settings and experimental methods for scanning

Once the sample is inside at high vacuum and titled the first calibration round is performed with the SEM in order to adjust the beam. The second round involves calibration of EBSD acquisition software (TSL OIM data collection 7). To start the first calibration stage, the beam is focused appropriately at a high magnification in order to obtain an adequate image of the microstructure of the surface. Commonly, a small deformity or dust particle was used as a reference in order to facilitate the process of visually seeing the difference between a well focused image, as opposed to a badly focused image. Next, three key beam tuning processes followed:

1. With a deformity in the beam focus, the "gun tilt" is toggled. As logically expected, this option tilts the field emission gun (FEG) which has a small impact on the electron beam trajectory through the magnetic field. From an experimental perspective, the gun is tilted in order to find the location of the maximum beam intensity on the sample.
2. Following the "gun tilt" option is the "gun shift" is next used for further calibration. Once the option is toggled on, the FEG will be shifted from side to side. In a well calibrated SEM, such a shift should have little to no impact on the focus point of the SEM. Although such a state was difficult to achieve, the beam was modulated such that little to no horizontal or vertical alternations are seen while the beam is shifting.
3. The final SEM tuning touch is the "stigmator" option. This option is used in order to improve the alignment of the SEM images obtained. The process objective is more easily explained by its failure. In a badly aligned set-

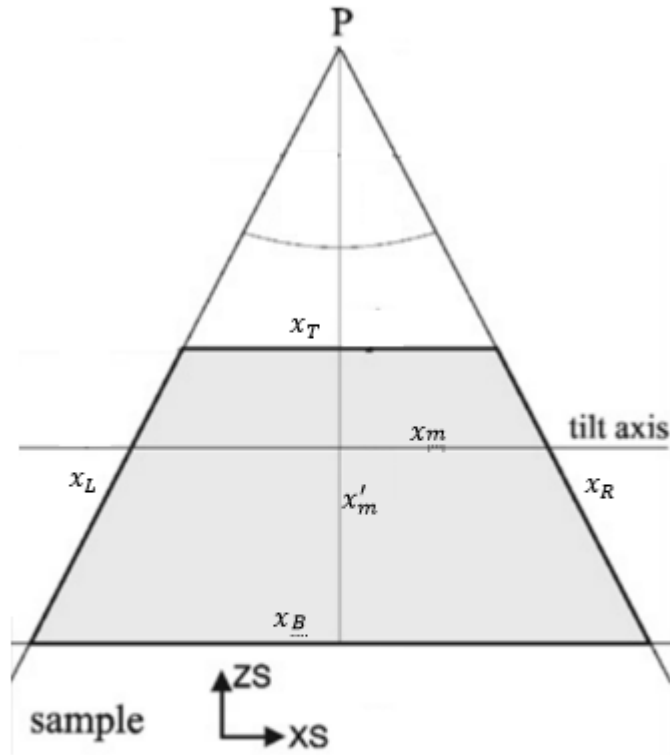


Figure 7: The rotational deviation of the beam across the tilted sample surface is presented in 2D. The grey surface represents the sample surface area of the analysed sample from the front at a 75° angle tilt (into the page). The electron beam raster scan is projected throughout the sample surface and starts at a theoretical pivot point P. The geometric lengths defined are as follows: x_L is the left length, and x_R is the right length, x_T and x_B are the lengths measured at the top and bottom of the sample respectively, finally, x_m and x'_m represent the middle length measured vertically and horizontally respectively. The deviations presented here are largely exaggerated for visual understanding of the distortion.

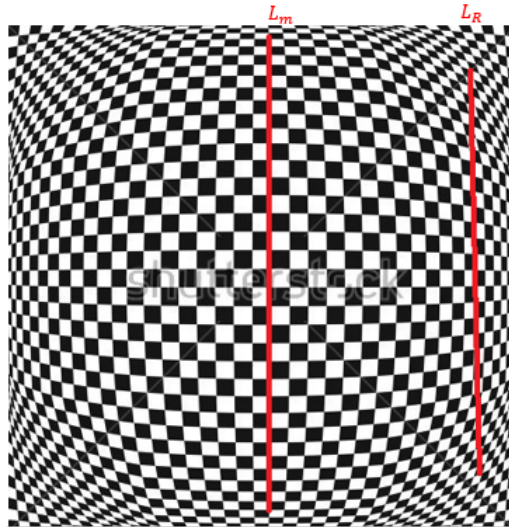


Figure 8: the fish eye effect is presented for an image which would have had geometrically equal squares if the effect were not present. This can be observed from the red line segments. L_m is the middle length, L_r is the length of the right segment. Deviations due to the effect are more prominent in corners than in the centre of the sample.

ting, changing the focus results in a horizontal or vertical blurred stretching of the observed image. This inaccuracy was fixed by using the "window" mode. This mode opens a small window within the SEM screen on which the entire electron beam is focused. Within this small window, the astigmatism was corrected by finding the least blurred image. As mentioned before, this procedure was always performed by placing the window beam on a small deformity or defect in order to be able to visually obtain an appropriate astigmatism. This procedure required high paced execution in order to minimize the sample damage.

At this stage, the SEM calibration settings are optimized, and the microscope was focused to the magnification required in order to take appropriate images of the sample. What follows is a description of the calibration of the various parameters used to acquire favourable quality electron back-scatter patterns(EBSP's)/Kukuchi bands and subsequently appropriate indexed data maps. Note that, emphasis is placed on the parameters most fundamental to this research since a complete sum up of all variables involved in EBSP pattern acquisition and processing would require a disproportionate extend of space in this report. For further information please contact the author(s):

1. For starters, the frame rate per second is to be selected. This rate quantifies the average speed of electron backscatter pattern(EBSP) data acquisition and is selected based on a predictive optimization of data quality and

the time limitations on experimental time frames. The highest possible option available is selected in the used data collection software. A second parameter which also affects the frame rate is the "image binning". This parameter quantifies how many data points are to be "binned" together in order to provide a single data point in an EBSP and is set to 8×8 . Taking into consideration both variables and by selecting the gain to be minimum(which gave the best quality EBSP's), leads to an averaged frame rate of ≈ 70 fps.

2. Background correction is required due to the low signal to noise ratio of EBSP's. To do this, data is captured for approximately $\times 10$ the frame rate per second. The background image is subsequently subtracted which greatly improves the captured EBSP by normalizing intensity gradients and improving band contrast.

As already mentioned, Hough transforms play a key role in successfully obtaining data. What follows is a description of a series of parameters used to tune the Hough transformation method itself:

1. The Hough transform convolutions mask is added as to correct the data in Hough space. It is mainly used because of the non-binary nature of EBSP patterns, as opposed to the patterns used in the examples above. The key requirement of the convolution mask is to correct the brightness peaks observed in the initial Hough transform received from EBSP's such that all true peaks have a "butterfly" like shape in the transform and intensity gradients are cancelled(see figure 9). The best size is related to band thickness and geometry of the data used. substantial improvement is achieved with a convolution mask of 9×9 (medium).

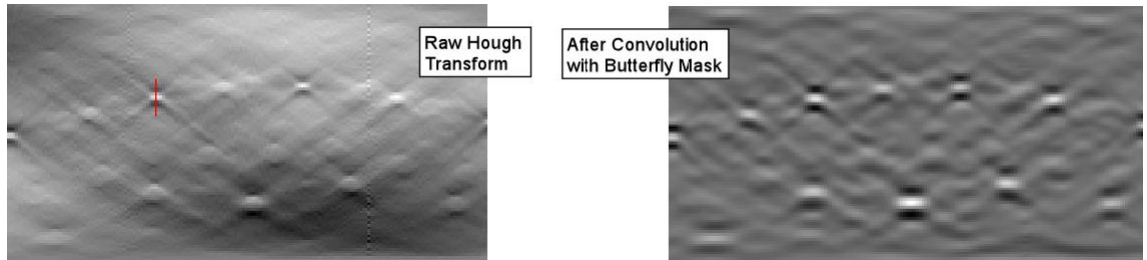


Figure 9: The difference of a typical Hough transform as obtained from EBSP patterns can be clearly observed before and after the convolution mask is applied. Max peak intensity points are much more easily found after the convolution mask is applied thus improving results[3].

2. The "minimum peak magnitude" and " minimum peak distance" of the Hough transform can be explained easily as follows: The intensity and inter distance requirements of the Hough transform peaks. If any peak

fails to satisfy the conditions set, it is not considered a peak and not incorporated into the numerical method used to produce indexed patterns. The minimal peak magnitude is set to 70, and the minimal peak distance is set to 20.

3. The "binned pattern size" is as mentioned before, characterized by the quantity of binned data points in Hough space in order to more rapidly quantify information. This parameter is set to 120 pixels.
4. the "theta step size" defines the accuracy of the angle of the associated Hough transform parameterization: $\rho = x\cos(\theta) + y\sin(\theta)$. Increasing the angle will reduce the time used to calculate the transform. For this research it is set to 0.5°
5. "Rho fraction" gives a direct indication of the magnitude of the obtained EBSP used to derive indexed bands. In other words, it determined how much of the transform data is used from the centre outwards in order to index data lines. For this research, 63% is found to give enough data.
6. Finally, the minimal and maximal peak count of Hough transforms, is set to 9 and 3 respectively. These parameters as reasonably implied define the number of Hough peaks required to define a sinusoidal curve in Hough space.

At this stage, most experimental parameters are set and ready for EBSD data collection. Final steps are concerned with using the stage control in order to switch the microscope controls to the EBSD software. Once this was done, the SEM software froze and TSL OIM analysis (EBSD software) was used to make a fast scan of the sample. Within this scan of the sample, an area was selected which was to be used in order to make EBSD raster scans. For the scans in this experiment, a step size of 1.5 μ m is used.

3.5 Samples analysed

During the manufacturing process of materials, grain size is a function of two key processes: nucleation and grain growth. Nucleation involves the amount of nuclei that are formed throughout the materials, whereas grain growth is associated with the growth of the individual nuclei. If grain growth is the prominent process, nucleation wouldn't be a prominent factor before the grains have extended over the volume of the material. On the contrary, if nucleation is prominent, extensive amounts of small grains will form before the surrounding grains have grown to cover the material. The high entropy alloy observed throughout this research have very large grains (of the order of a few millimetres) and consist of the following elements: $Al_{0.1}CoCrFeNi$

The high entropy alloys researched and the mechanical conditions which they have been subjected to are presented in table 1.

mechanical condition	temperature treatment	subjected force(N)	number of cycles in fatigue test
non-fractured	as cast	979N	$N > 10^7$
non-fractured	400h at 700°C	2780N	$N > 10^7$
fractured	as cast	3114N	$N = 552640$
fractured	400h at 700°C	3114N	$N = 1471266$
fractured	as cast	3336N	$N = 238646$
fractured	400h at 700°C	3336N	$N = 316608$

Table 1: The presented data shows 3 differing conditions which the materials have been subjected too: weight load, temperature treatments, number of cycles of tensile tests.

4 Method 1: merging of data sets

4.1 Scanning method and results

In order to merge EBSD data sets, scans were selected in 3 batches of 3 scans which are made vertically above one another with an overlap of $20\mu m$ such that the merging process can be performed visually with appropriate accuracy(see figure 10).

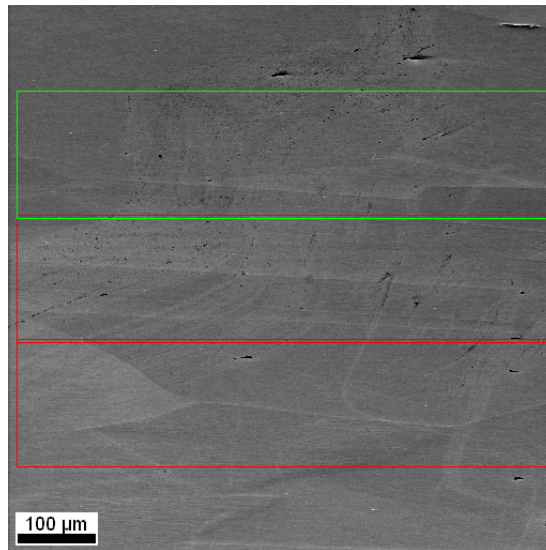


Figure 10: vertical scans sequence for merging of data sets. These scans are made at a magnification of 100 and a step size of $1.5\mu m$

Such a scanning sequence is performed 3 times horizontally as well such that a 3×3 "matrix" system of images is produced which can be merged together into a single EBSD map using TSL OIM analysis software(version 8). The objective

of this merging, processes, is to provide maps which cannot be distinguished into their independent components of the "matrix", such that a microstructural analysis provides highly accurate information. The resulting merged data set Inverse Pole figure(see page 19 for more information regarding inverse pole figure diagrams) is presented in figure 11 for the following sample: non-fractured, 400 h 700°C 2780 N non-fatigue affected area.

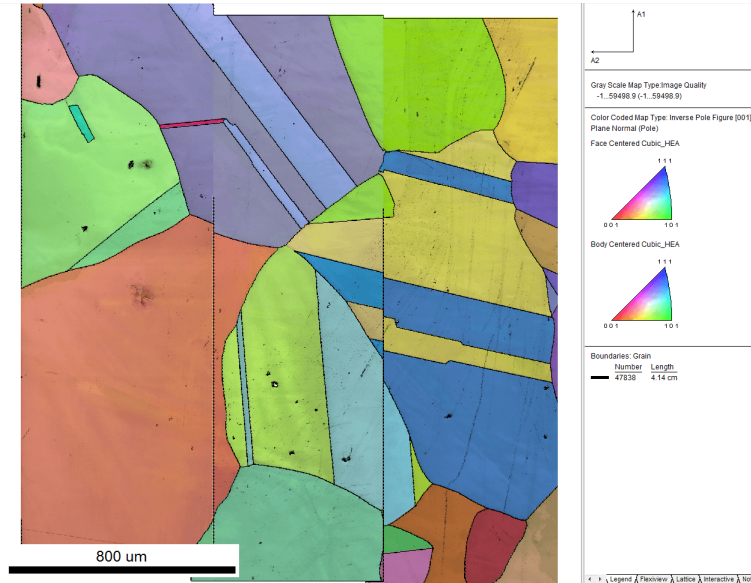


Figure 11: [001] Inverse pole figure of 9 merged data sets. All other types of maps used to describe the mechanical properties of the alloys with similar magnification will result in a similar geometric shape.

4.2 Discussion and methods for improvement

EBSD technology faces various limitations when used to analyse merged data sets.

It is quickly observed from figure 11, that vertical merging methods are extensively accurate because the vertical entries of the "merging matrix" all align geometrically. The merging process required little to no more than the information regarding the offset of the x which is 0um, the y overlap which is 20um and the size of the scan area which is 680 um. Using this information vertical data set merging can be performed with high precision on a scientific standard for further analysis regarding mechanical properties. On the other hand, horizontal merging proved to be more challenging. It is observed, that the merging process leads to irregularities in the OIM map and that regardless of the positioning of the two data sets, perfect alignment of all grain boundaries as well as the imperfections and scratches is impossible regardless of the fact that the image dimensions are identical. This effect can be traced back to

the magnification used in the microscope and the previously theorised sources of image distortion effects in EBSD technology: the fish eye effect and the trapezoidal distortion.

Thus in order to improve the alignment of horizontal merging of data sets, both distortions are to be quantified as a function of the scanning magnification used and minimised such that the effects become insignificant in merged maps

4.3 Quantifying EBSD distortions

It is known from theory that the distortions are directly a function of the magnification selected[6]. In order to minimise the distortion, the magnification for which a minimum horizontal distortion exists where to be found. To do so, a grid system was scanned at various magnifications with 3 different methods:

1. tilted using the SEM imaging(XHD) in order to measure the trapezoidal distortion
2. tilted using the EBSD imaging(DC) which can also be used to measure trapezoidal distortions as well as any differences that may exist between SEM and EBSD fast scans.
3. non-tilted using SEM camera in order to measure the fish-eye effect

The grid system itself has various different smaller grids which are composed of differently sized squares. Various different measures of the length of these squares have been made as presented in the theory in order to quantify any irregularities. Figure 12 presents one of the areas of the grid system that was used and is followed by various figures which present the distortions at various different magnifications.

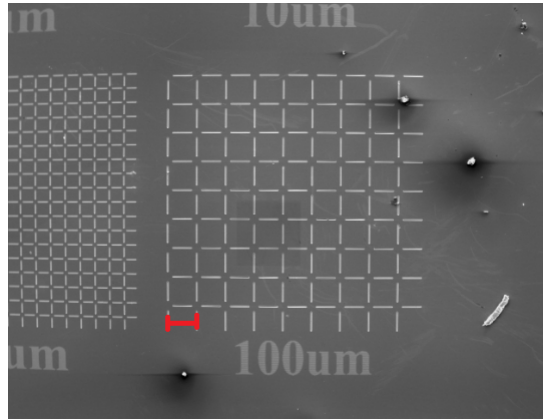
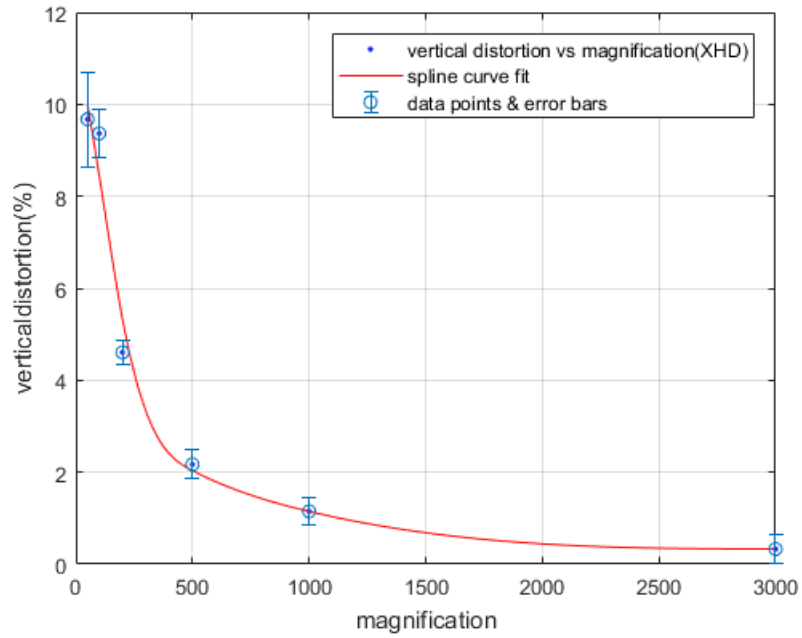
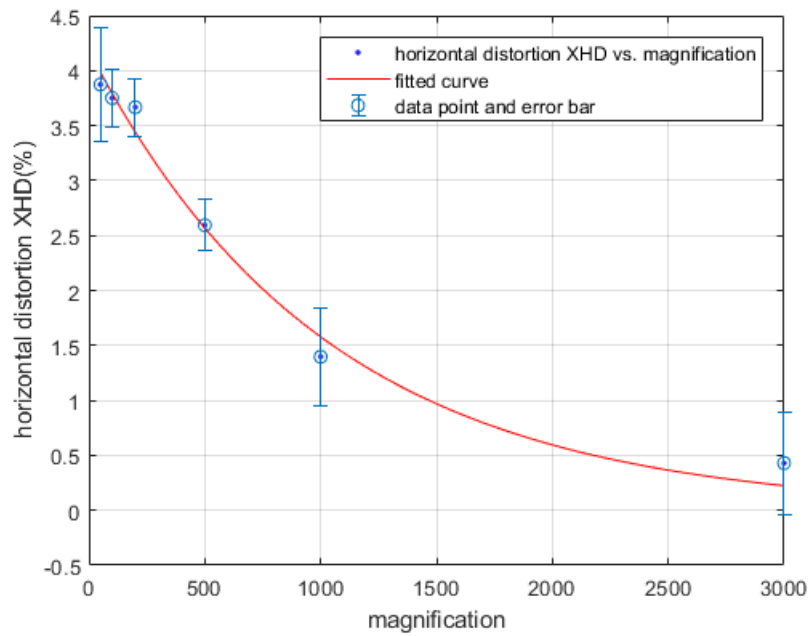


Figure 12: SEM image of the $100\mu\text{m}$ grid in the grid system at a $65\times$ magnification. In this system, the red line presents a single side of a $100\mu\text{m}$ square.

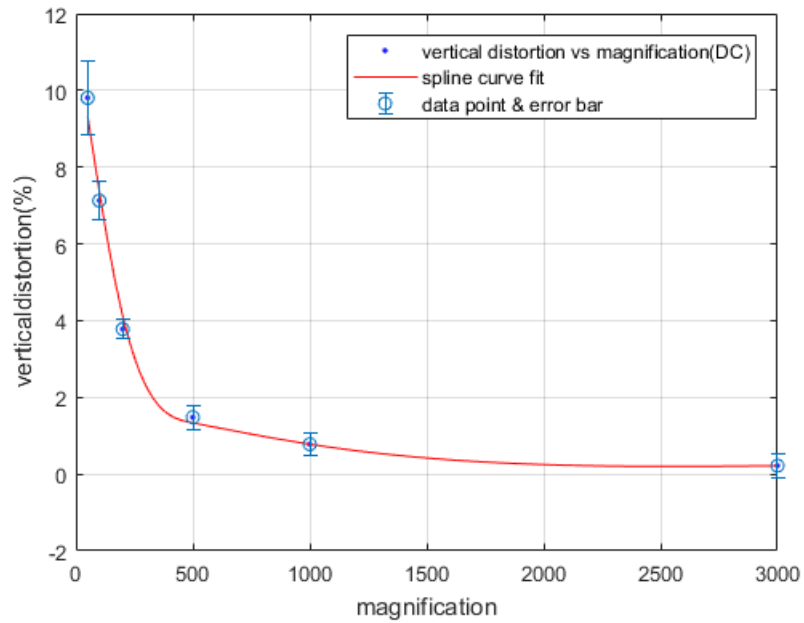


(a) vertical distortions vs magnification using SEM software for image capturing

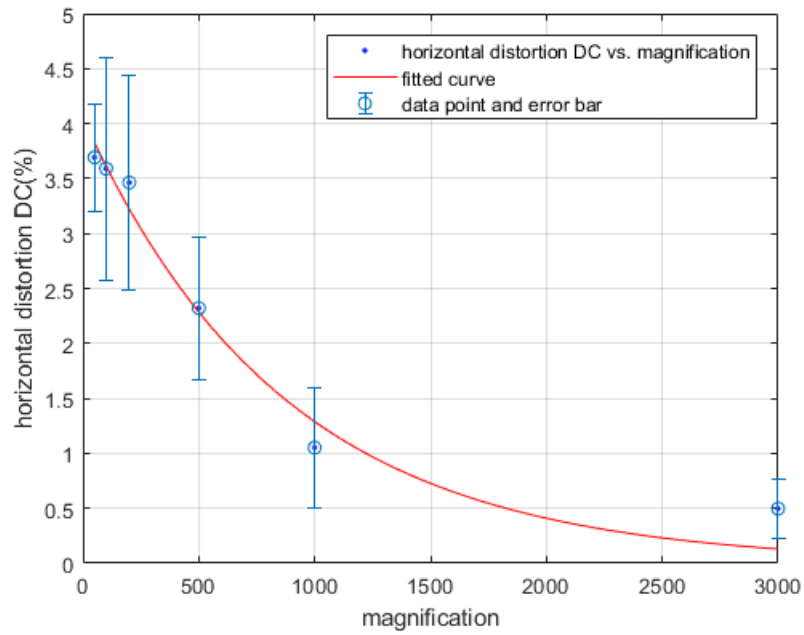


(b) horizontal distortions vs magnification using SEM software for image capturing

Figure 13: tilted sample stage where 20 images are taken using SEM software(XHD)

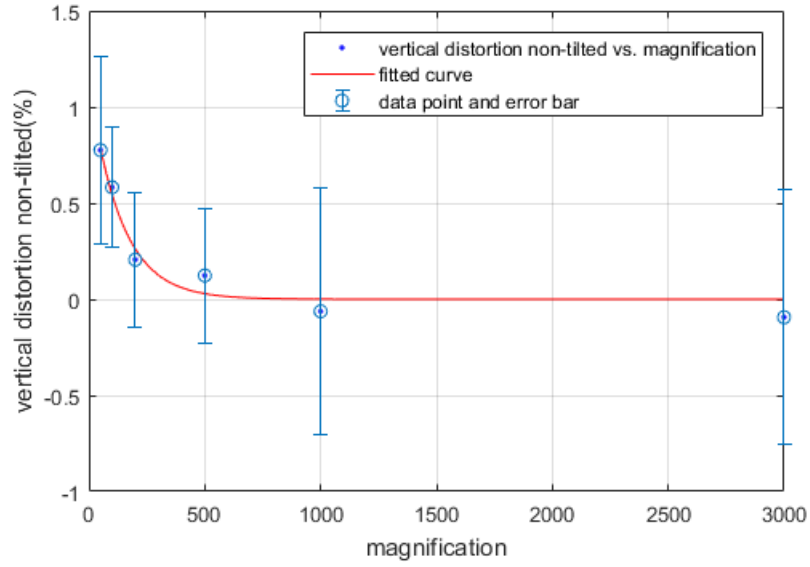


(a) vertical distortions vs magnification using EBSD software for image capturing

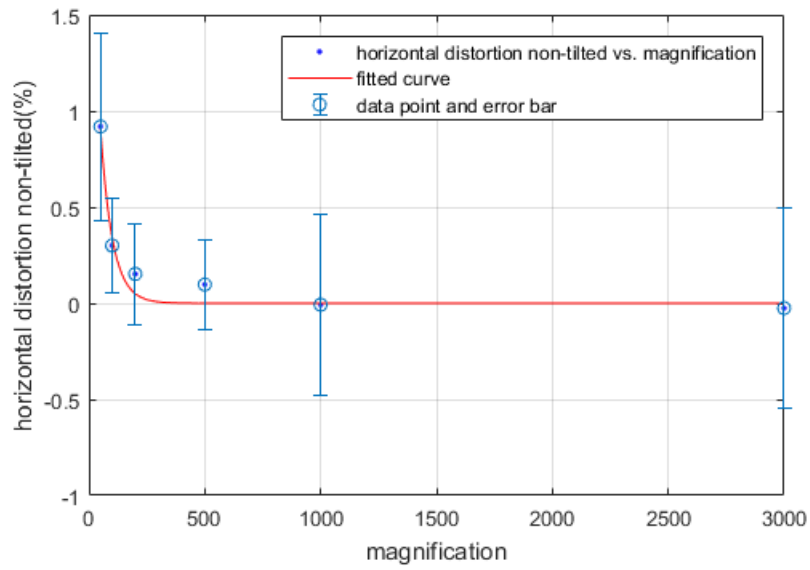


(b) horizontal distortions vs magnification using EBSD software for image capturing

Figure 14: tilted sample stage where images are taken using EBSD software(DC)



(a) vertical distortions vs magnification of the sample when not tilted



(b) horizontal distortions vs magnification of the sample when not tilted

Figure 15: non-tilted sample stage where images are taken using the SEM camera(XHD)

4.4 Final discussion for merging methods

The distortion graphs presented by figure 13 and 14 both provide very similar behaviour, which is not surprising and helps to confirm that there was no systematic difference present when collecting images from the SEM software, to

the EBSD software. For this reason, both data sets will be discussed together from here on.

Both diagrams show that horizontal distortions(13b and 14b) measured are key too providing proof of the magnification of the trapezoidal distortion. From the figures, it appears that the distortion never really disappears, but gets close to vanishing once the magnification is over ≈ 2000 (distortions smaller than 0.4%). This magnification is extremely high for the proposed observations, and would not provide appropriate results regarding the mechanical properties of the material, unless the "merging matrix" was to become much bigger, which would be contradictory, since then the infinitesimally small distortions would simply add up during the merging process and would eventually produce a visual trapezoidal distortion once more.

An interesting and unexpected finding is that both data sets also show that a vertical distortion is present in the examined grid(13a and 14a). This distortion, is however not present when the data sets are merged together. If this distortion was present in the obtained data sets, vertical merging would fail for similar reasons as horizontal merging.

In order to understand this, figure 10 is to be examined. In figure 10, the EBSD image scan system is used to provide the user with an area preview where scan regions can be selected. In the EBSD fast scan, the vertical distortion is present, however, since the scan areas selected are exact squares, this distortion is not visualised in EBSD data maps. What is observed in EBSD data maps(without the user being aware of it) is that the magnification of the sample is slightly higher at one end of the scan than at the other, thus the magnification of a scan is not a constant value, but is a low gradient linear function. The consequence of such behaviour is, that in EBSD collected data coordinates of the points where EBSD measurements were performed are recorded wrongly with a constant distance between them. In reality, the distance between measured points is not constant and slightly depends on local SEM image distortion. Due to the fact that EBSD analysis software simply assumes a constant distance between all neighboring points in the map, simple merging of maps collected at low magnifications is not possible without discrepancies in distance.

Figures 15a and 15b both show similar graphs as expected. This is mainly because, as can be observed from figure 8, the fish eye effect should be the same in both vertical and horizontal directions.

On top of this, it must be mentioned that the magnification dependence of the fish eye effect presented in both figures 15a and 15b drops much quicker than the trapezoidal or vertical distortions and becomes non-existent beyond magnifications of ≈ 500 . Any imaging experiments at magnifications below this value will experience both the trapezoidal distortion, as well as the fish eye effect whereas experiments beyond this magnification will only suffer from the trapezoidal distortion who's magnitude depends on the selected magnification.

For the purpose of providing an accurate measurement of the microstructural features of large areas(few mm^2) of the samples tested in fatigue, this method has not been used any further in this report. Instead, low magnification big scans where used. These scans weren't able to carry to completion as many

indexed data points in a single raster scan as the merging method could. It will however disqualify any issues related to the merging method such that there does not need to be any further research on the method itself before performing the experiment and further leading the way for the analysis of mechanical characteristics. It should however be noted, that the OIM maps collected by this method, still suffer from the fish-eye and trapezoidal distortions, although not visible on the OIM maps.

5 Method 2: Large scans

5.1 Analysis of OIM measurements

The software to be used (OIM analysis 8) offers a vast spectrum of options for analysis and presentation of the characteristics of the materials examined. The methods used are explained in two different subsections: first the cleaning process, and next map types which have been used for analysing the microstructural characteristics:

5.1.1 Data cleaning process

1. **grain CI standardization**

This is a cleanup technique used to normalize the CI value within a grain. CI values are based on the difference between the number of votes of the top indexed solution and second best solution. Low CI values do not count for direct proof that a certain point is incorrectly indexed, but rather a low confidence of that point. At grain boundaries the case is often experienced, where due to the boundary, indexed patterns alter which leads to a low confidence, but does not cause a data point to be wrongly indexed. Similarly, if a single point is found to have a very low confidence index, while being surrounded by points of high confidence index, it can be considered with a high probability to be an indexing error.

If the orientation of such data is similar to that of the surrounding data points CI standardisation can be used to normalise the CI value. Thus, the analysis, allows to clean up data which is most likely to be correct based on their orientation while leaving points with a vastly different orientation. In the data sets used, the tolerance angle is set to 5° and the minimum grain size (which defines the minimum number of points required to define a grain) is set to 3.

2. **Neighbour orientation correlation(NOC)**

The NOC clean up method analyses every sample point and tests them for 3 conditions. The first condition tests the CI value. After this is done the orientation of all neighbours is checked and compared to the data point being tested. The requirement can be selected by choosing the appropriate clean up level. For a clean up level 0, all surrounding orientations must be different, for a clean up level 1 all but a single orientations must be

different and so on up to clean up level 5 (which is the maximum number of available points considering the geometry of the analysis method). If the number of neighbours around the data point is different the last condition is executed. This step tests how many of the surrounding neighbours have similar orientation to the pre-selected tolerance angle of 5° . For cleanup level 1 all but one data points need to have similar orientation to one another, and so on. If the final condition is also satisfied, then the orientation of the data point is changed. This method works well in order to clean up badly indexed data points.

3. low CI values

All values with low confidence index are likely to be the result of miss-indexed data points, as a result of which the data is not reliable. In order to prevent highly inaccurate data from dominating the results, all entries with a confidence index smaller than 0.3 are excluded from data maps.

5.1.2 Map types

1. inverse pole figure map(IPF)

In this map a colour spectrum is used in order to define which crystallographic direction is aligned with a user selected sample direction. The IPF diagrams presented in this paper are [001] meaning that the user selected normal is in the z - axis of the sample (normal to the sample surface). The axis are defined only in figure 11.

2. phase map

This map type is used to show the presence of different phases in each type of analysed sample, and their location.

3. IQ map

IQ maps represent the image quality (IQ) at all indexed data points. IQ itself is defined as the sum of peaks detected in Hough space which contain information regarding quality of the EBSP. Bright data points present high IQ value and dark points present low IQ value.

4. Kernel average misorientation

This map type uses a kernel, which consists of a group of indexed data points around the measured data point in order to measure the points misorientation when compared to the surrounding neighbours. The size of the Kernel can be user selected and is chosen to be 2 (second neighbours). In order to prevent the KAM information from becoming unreasonable, grain boundaries and defects are considered by selecting the maximum misorientation acceptable to be 5°

5. grain average misorientation map

The average misorientation of each point is calculated using a kernel allowing for grain orientation distributions to be visualized.

6. Schmid Factor

The Schmid factor distributions throughout the grain is presented based on the selected stress direction. The stress values (based on the used axis defined by the software) is in the y-direction: $\sigma = \sigma_y$. The Schmid factor was calculated on base of the FCC grain orientation towards this stress direction.

7. Grain orientation spread

The grain orientation spread map (GOS) colours an entire grain as one single colour. The colour is determined as follows: the average orientation of the grain is calculated. The misorientations of each point with respect to the average orientation is calculated. The average of the misorientation angles are calculated and assigned to the grain.

8. Grain reference orientation deviation

This map will be used to find where local misorientations are within a grain. In order to do so, the average orientation within a grain is calculated. The intensity at each point is determined by the misorientation of that point with regards to the average grain orientation

5.2 EBSD maps and results

What follows are various sections containing the different maps of each of the samples followed by the results which these maps provide. The order of the sample types is related to the subjected force applied (from smallest to biggest), as presented in table 1. The maps are organised such that the fatigue testing force is subjected in the reading direction (in the *A2* direction as presented in figure 11).

For each sample section analysed 2 faces are required to present all maps. The order is presented as follows:

1. face 1: Inverse pole figure, phase and image quality maps
2. face 2: Schmid factor, Grain orientation spread, Kernel average misorientation and finally Grain reference orientation deviation.

5.2.1 Non-fractured, as cast, 979N, fatigue affected area

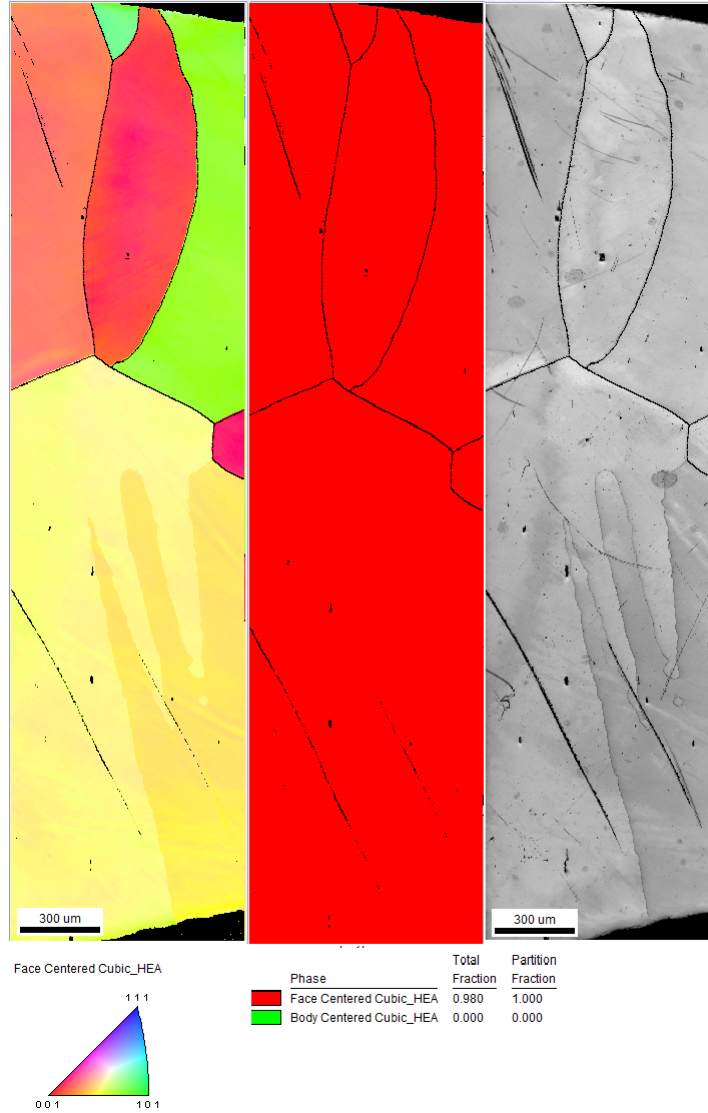


Figure 16: The first figure from the left presents the [001] inverse pole figure, the middle figure presents the phase diagram, the right figure represents the image quality map

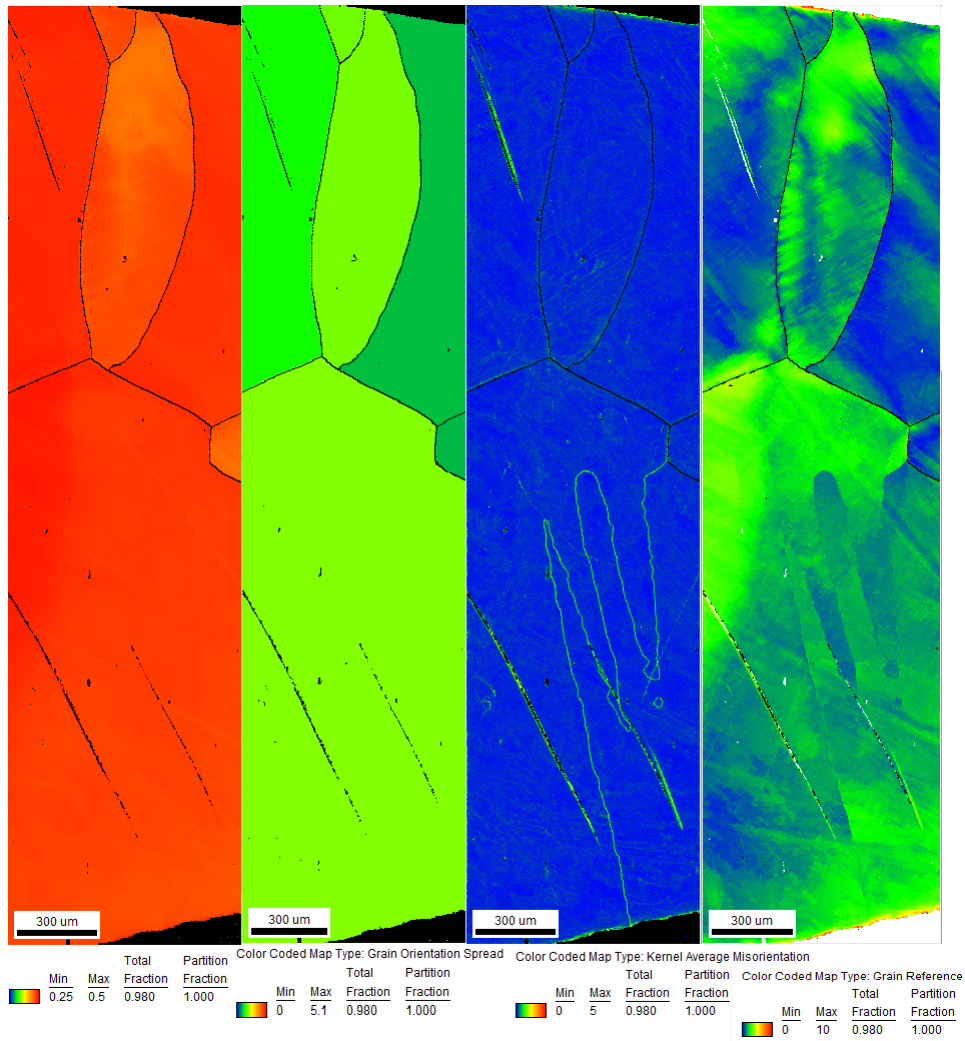


Figure 17: The first figure from the left presents the Schmidt factor map, the second figure presents the grain orientation spread, next is the Kernel average misorientation, and finally the Grain reference orientation deviation

5.2.2 Non-fractured, as cast, 979N, non-fatigue affected area

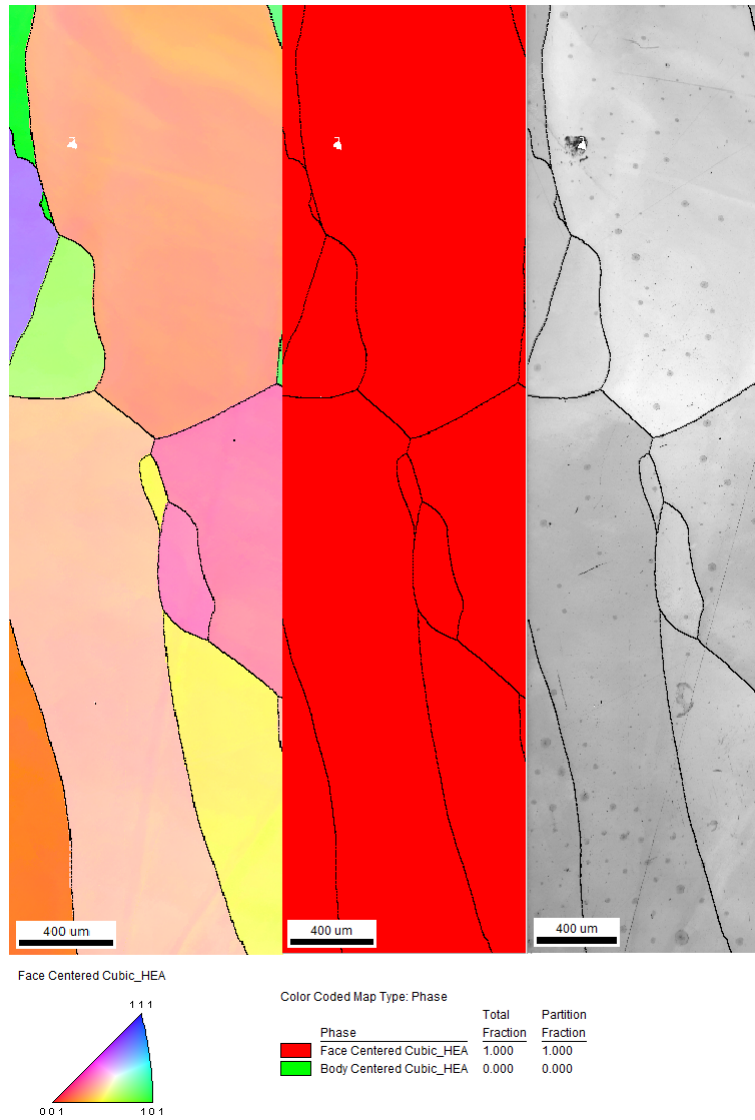


Figure 18: a)inverse pole figure b) phase map c)IQ map

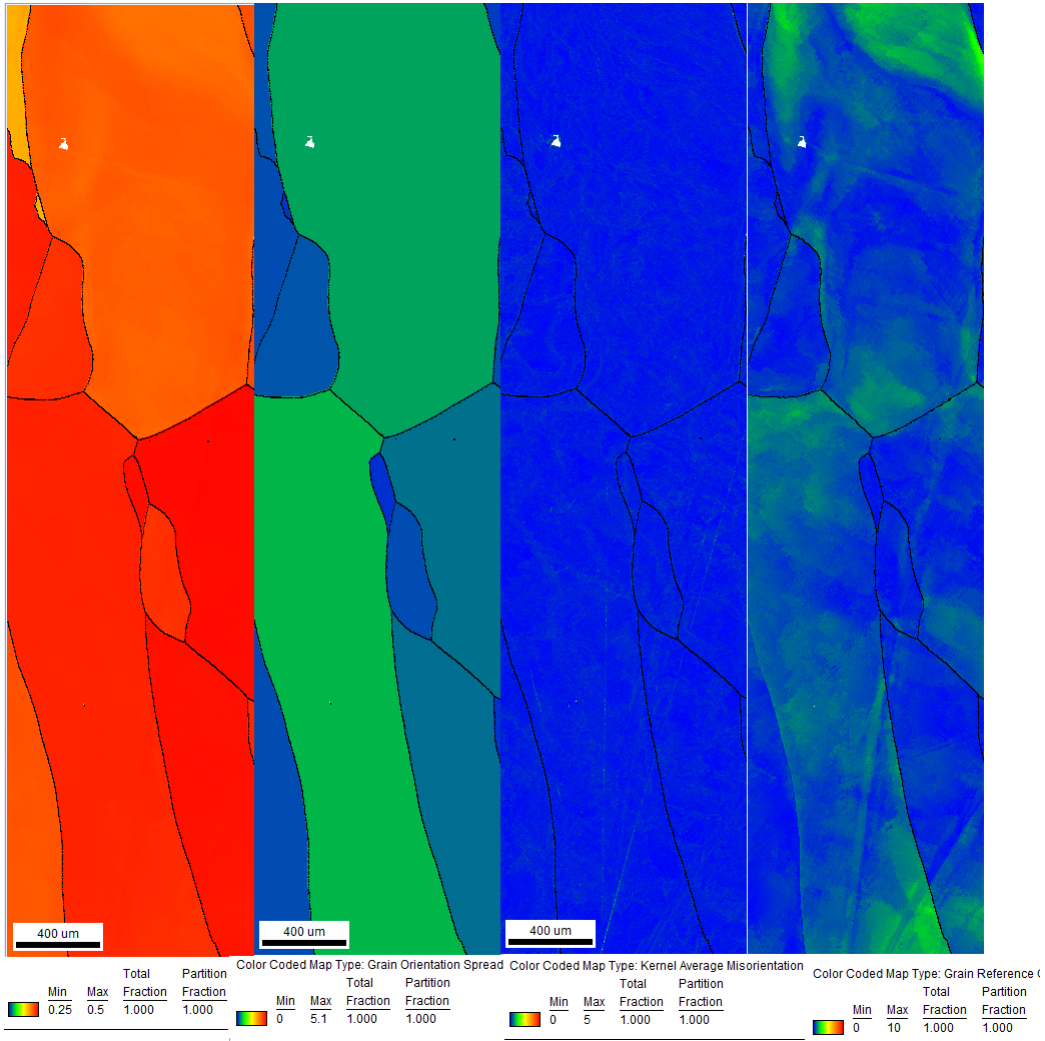


Figure 19: a)Schmidt factor map b) grain orientation deviation c) Kernel average misorientation d) grain reference orientation deviation

5.2.3 Non-fractured, 400h at 700°C 2780 N, fatigue affected area

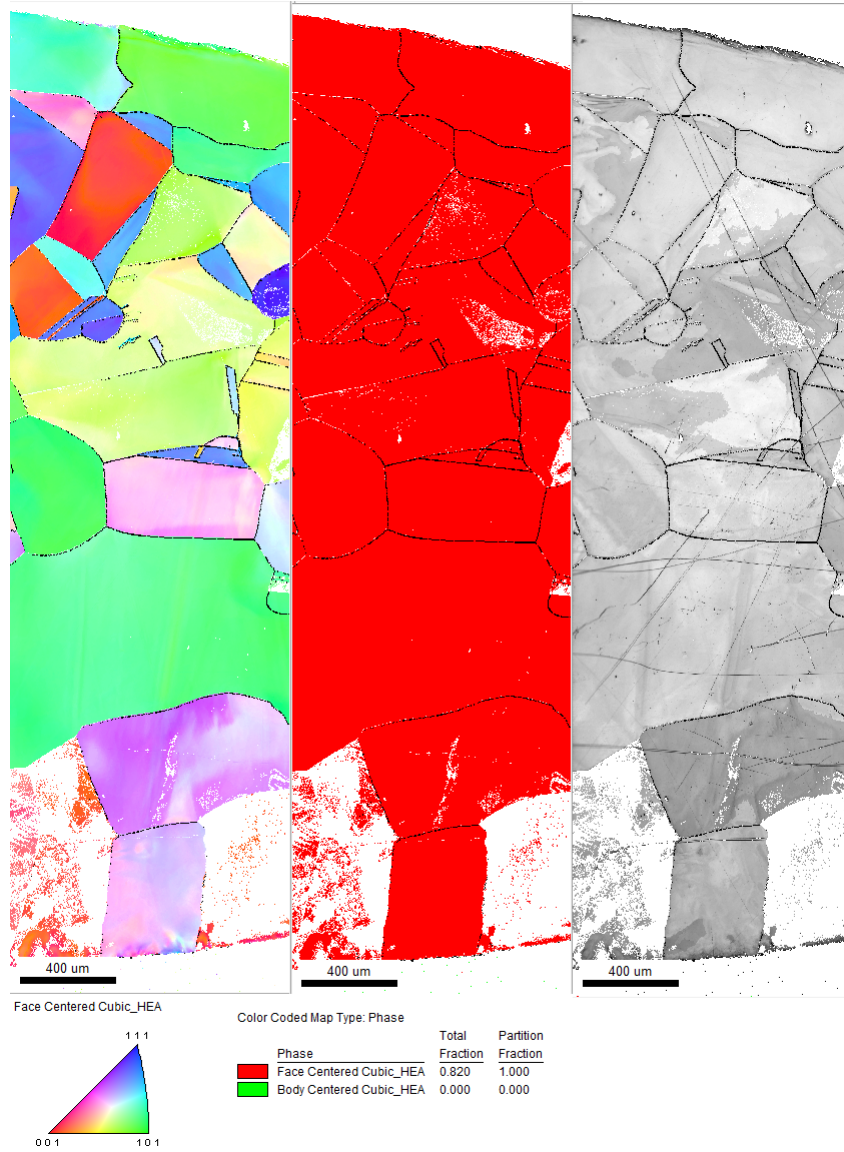


Figure 20: a) inverse pole figure b) phase map c) IQ map

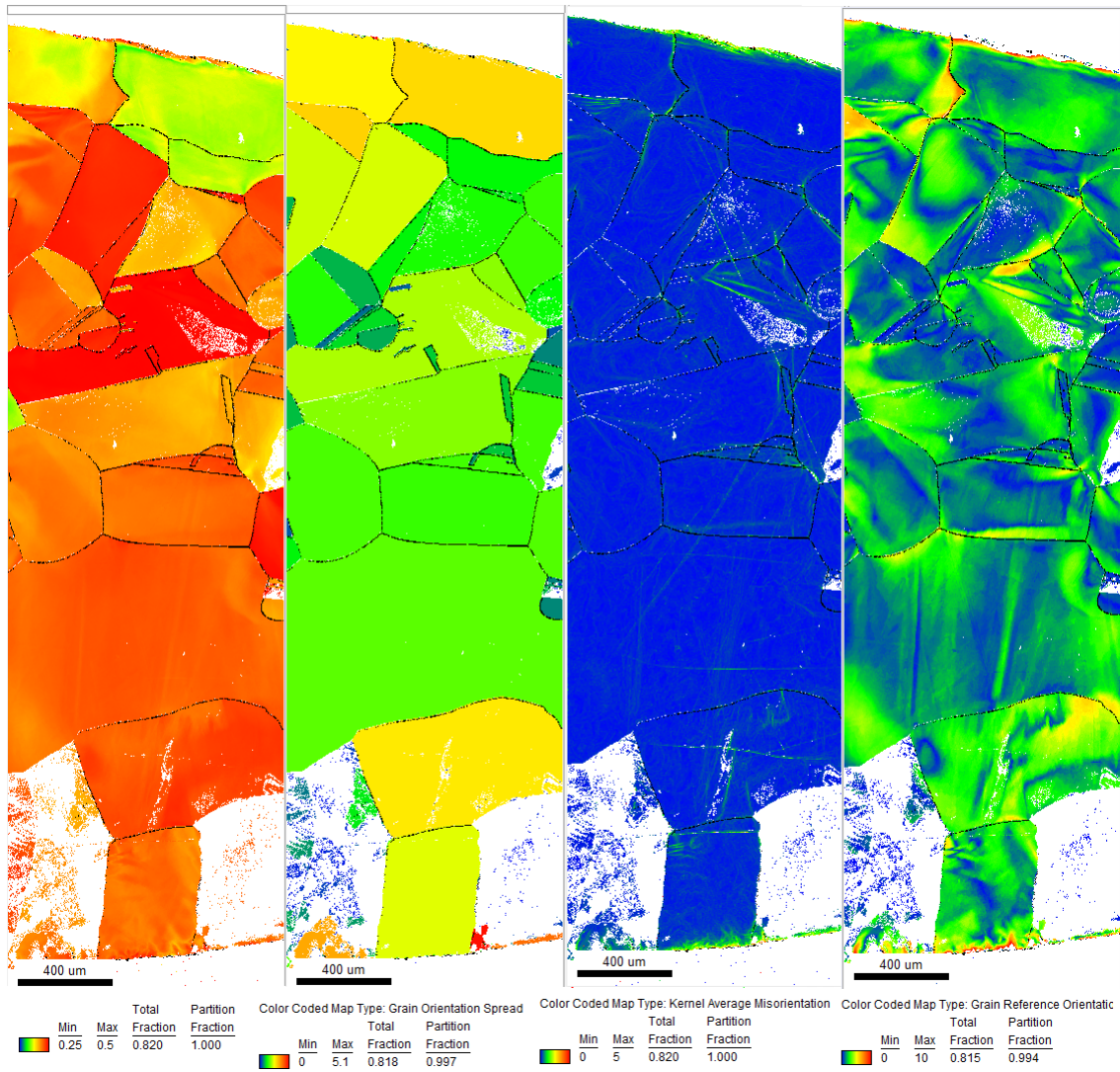


Figure 21: a)Schmidt factor map b) grain orientation deviation c) Kernel average misorientation d) grain reference orientation deviation

5.2.4 Non-fractured, 400h at 700°C 2780 N, non-fatigue affected area

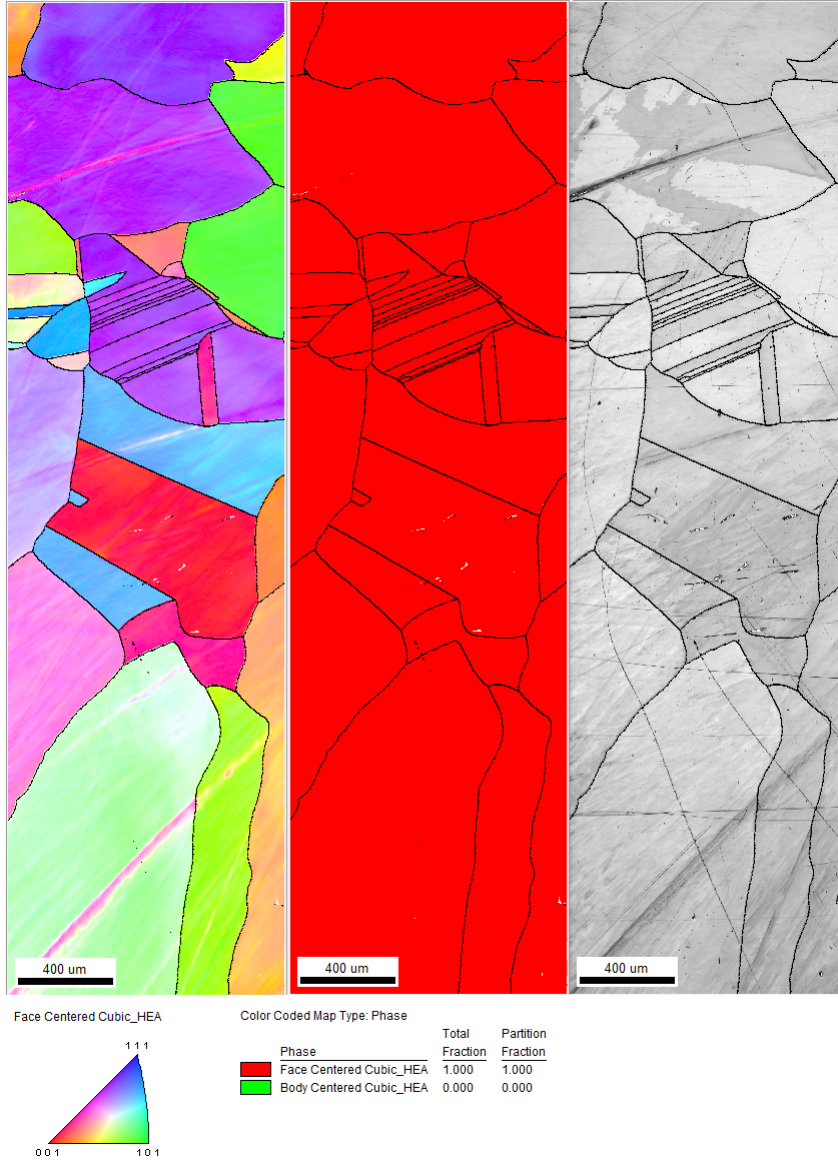


Figure 22: a) inverse pole figure b) phase map c) IQ map

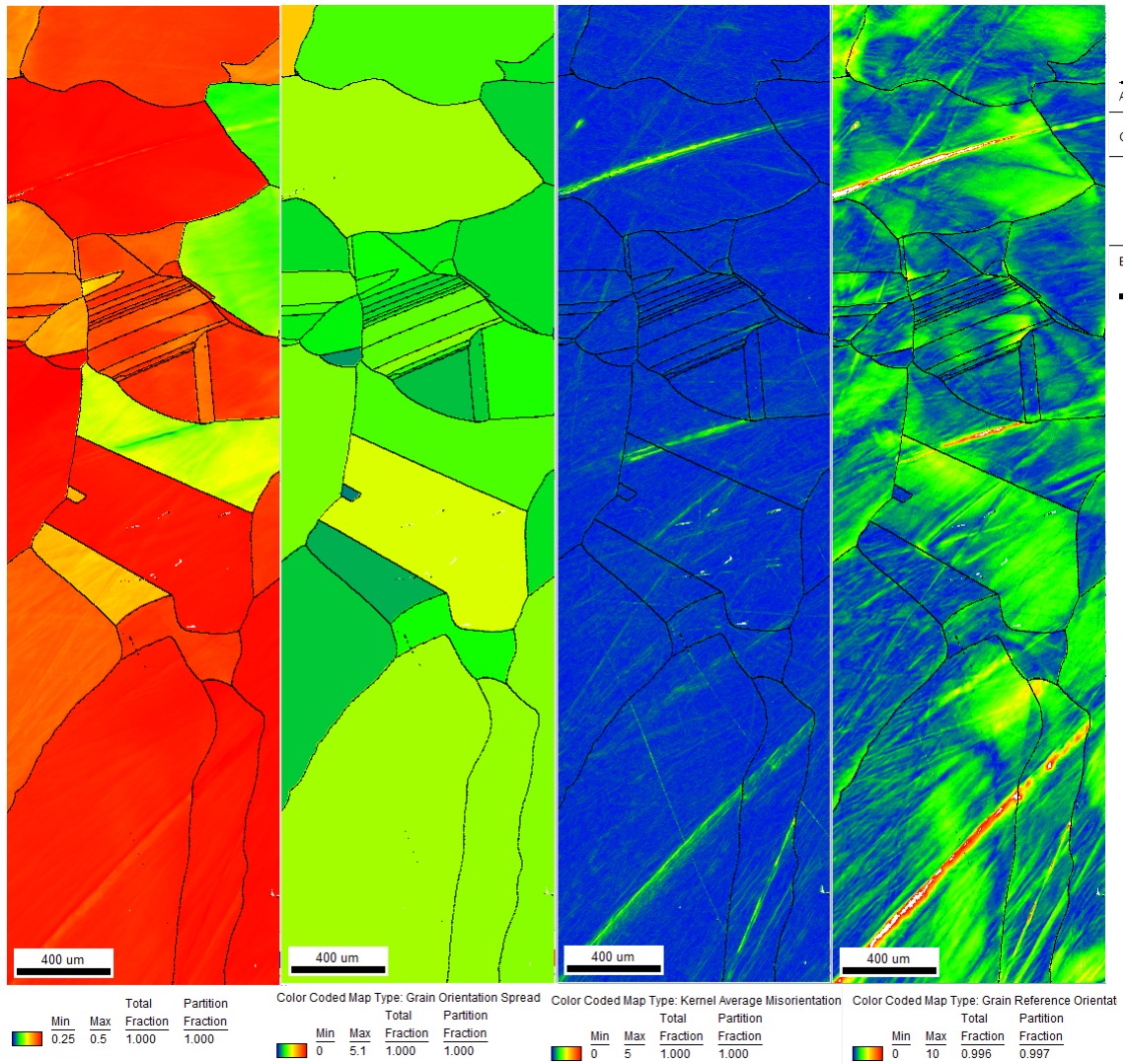


Figure 23: a)Schmidt factor map b) grain orientation deviation c) Kernel average misorientation d) grain reference orientation deviation

5.2.5 Fractured, as cast, 3114N

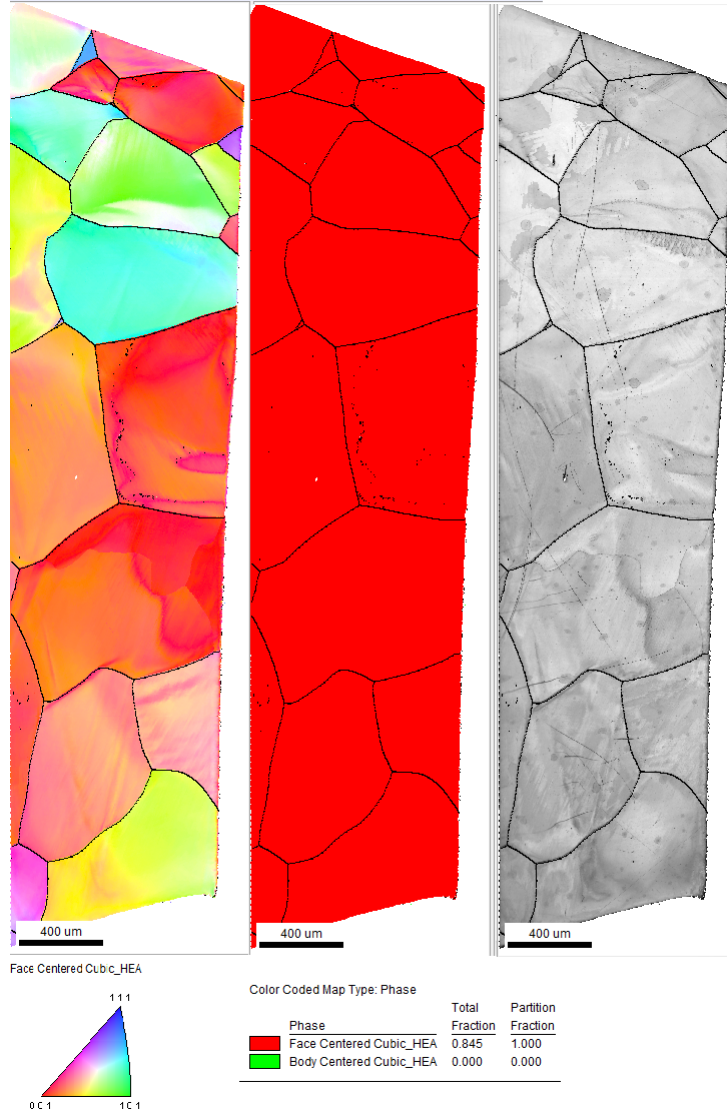


Figure 24: a) inverse pole figure b) phase map c) IQ map

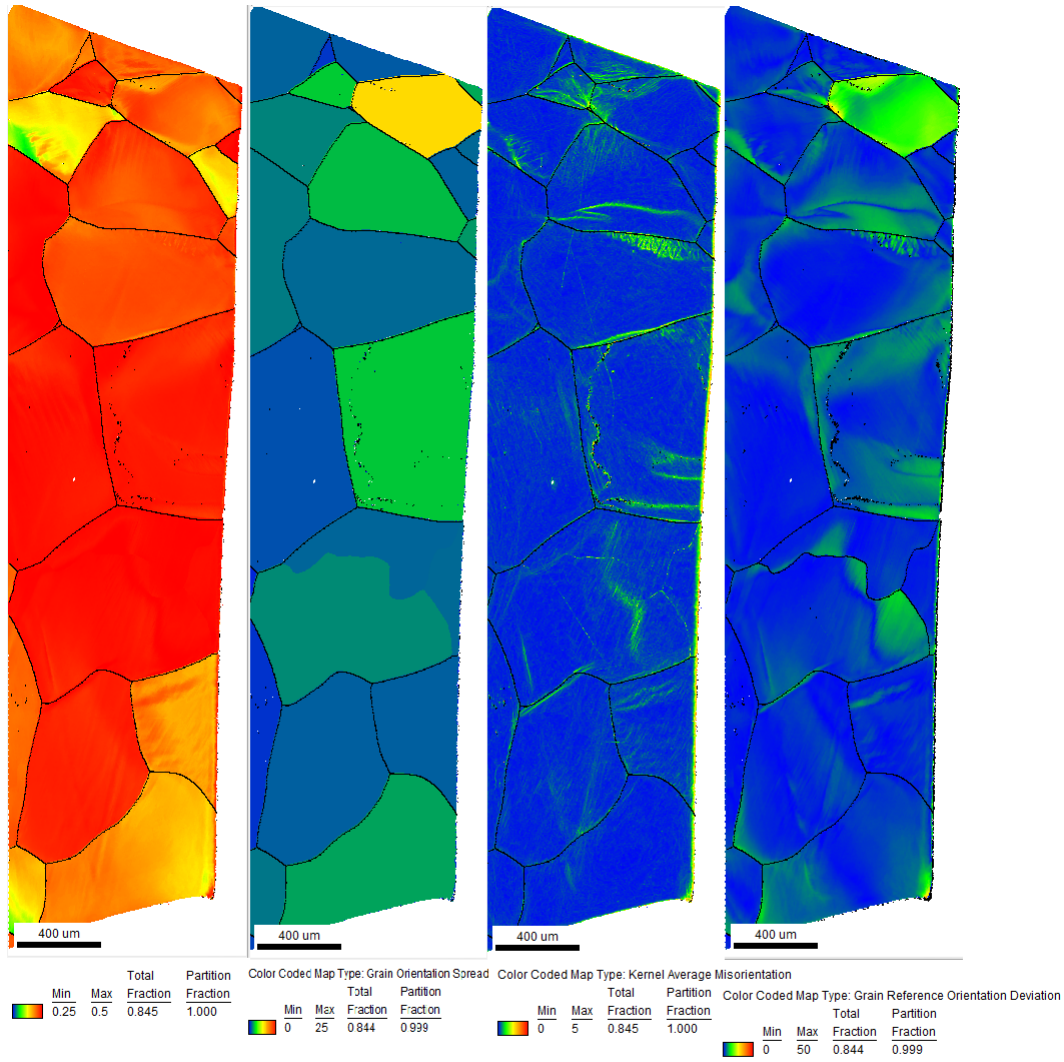


Figure 25: a)Schmidt factor map b) grain orientation deviation c) Kernel average misorientation d) grain reference orientation deviation

5.2.6 Fractured, 400h at 700°C 3114N

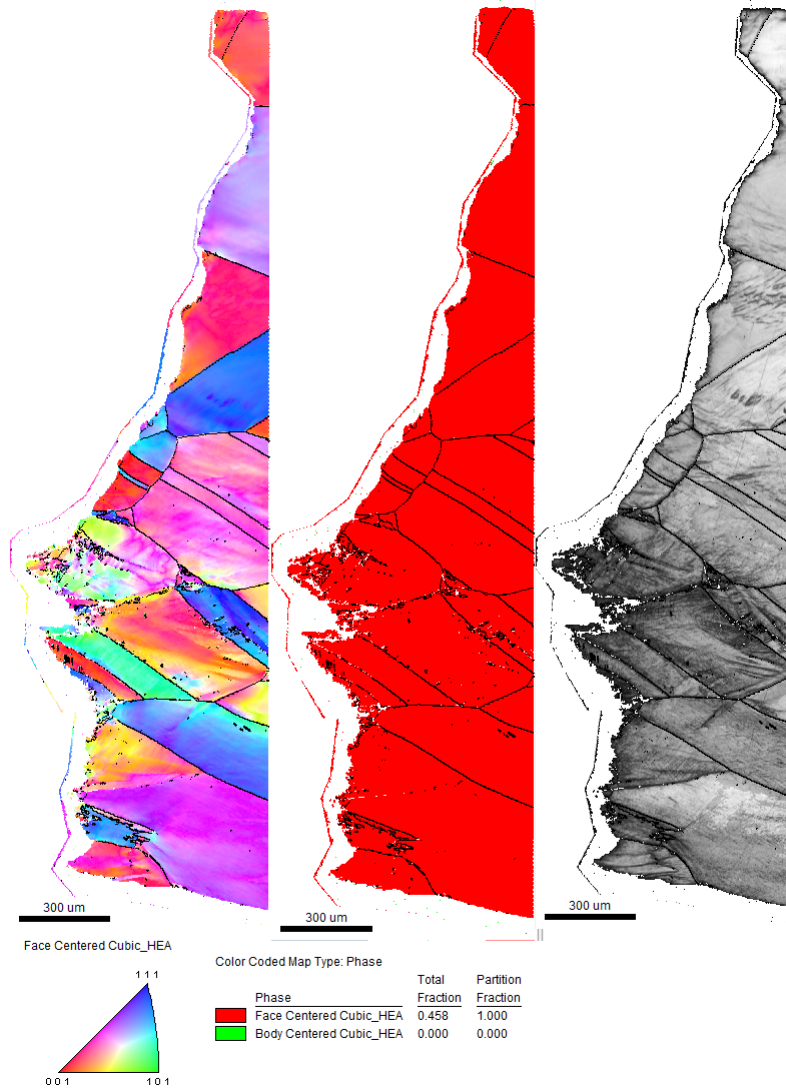


Figure 26: a) inverse pole figure b) phase map c) IQ map

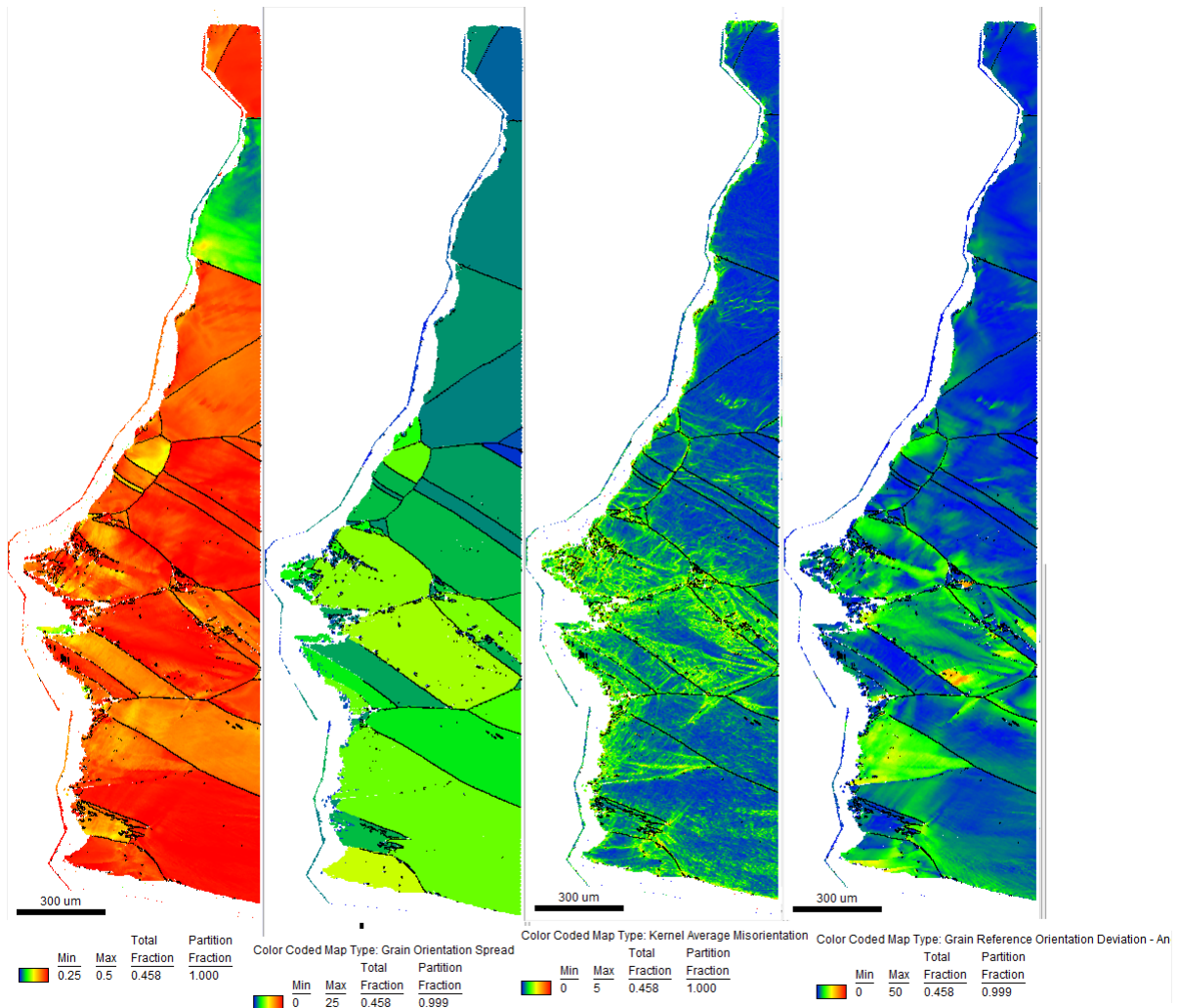


Figure 27: a)Schmidt factor map b) grain orientation deviation c) Kernel average misorientation d) grain reference orientation deviation

5.2.7 Fractured, as cast, 3336 N

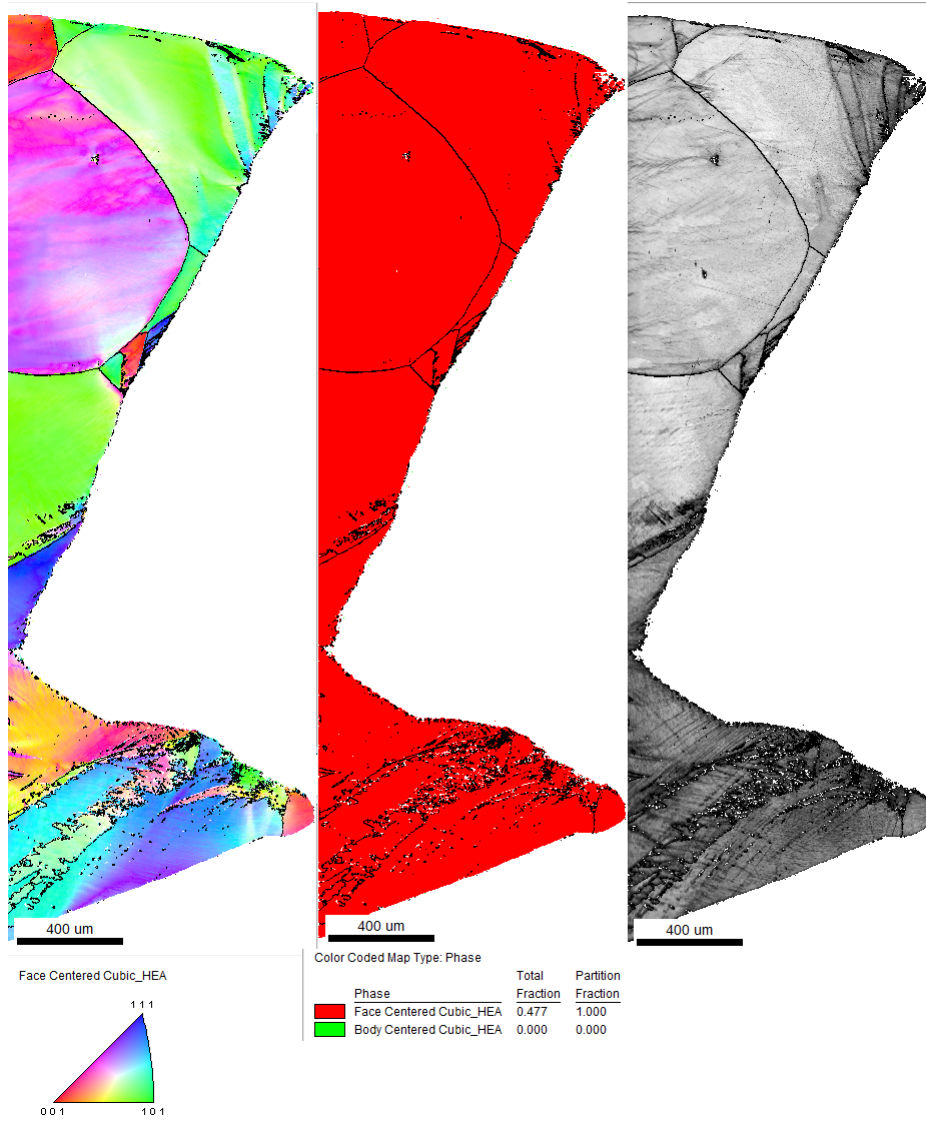


Figure 28: a) inverse pole figure b) phase map c) IQ map

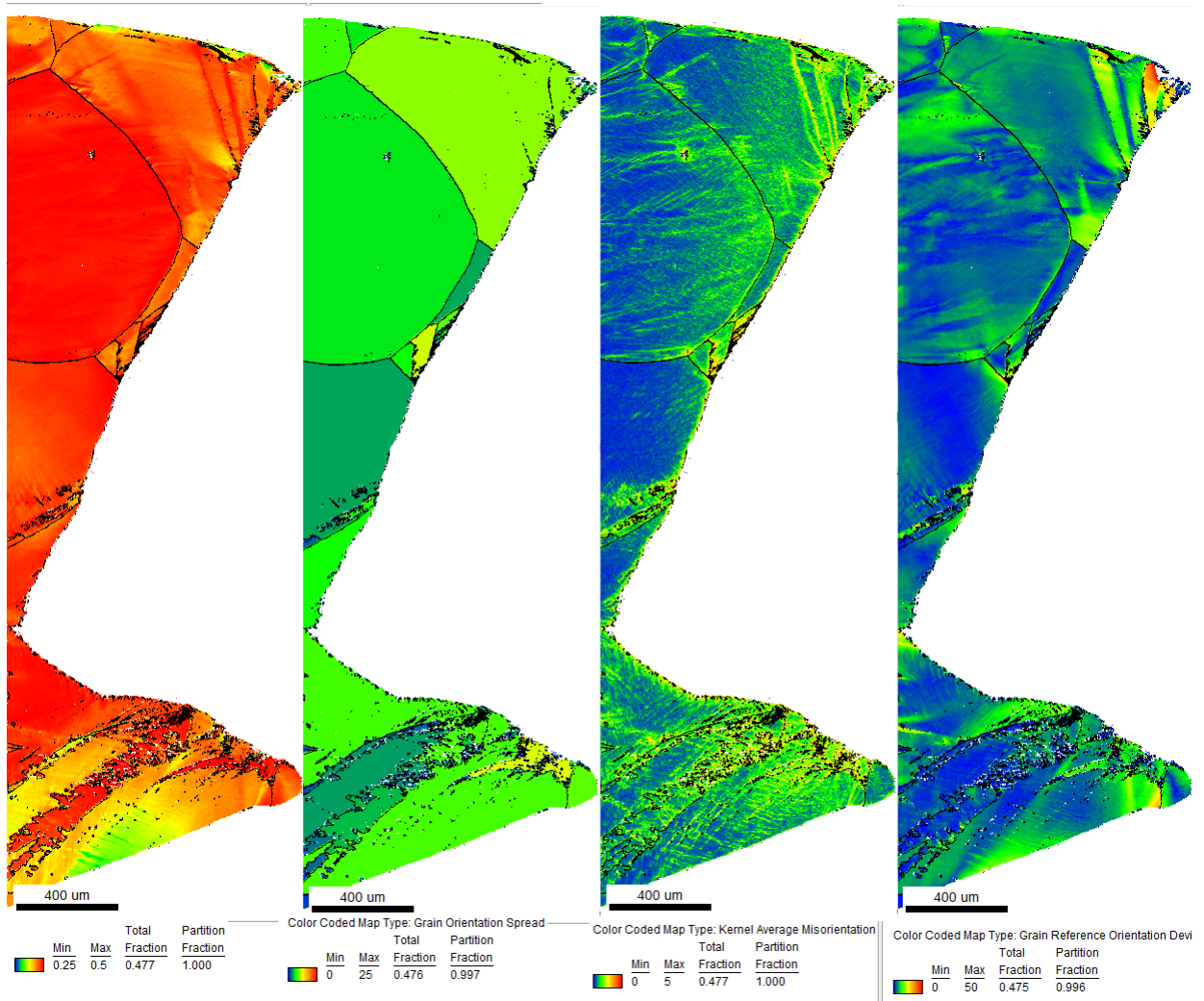


Figure 29: a)Schmidt factor map b) grain orientation deviation c) Kernel average misorientation d) grain reference orientation deviation

5.2.8 Fractured, 400h at 700°C 3336N

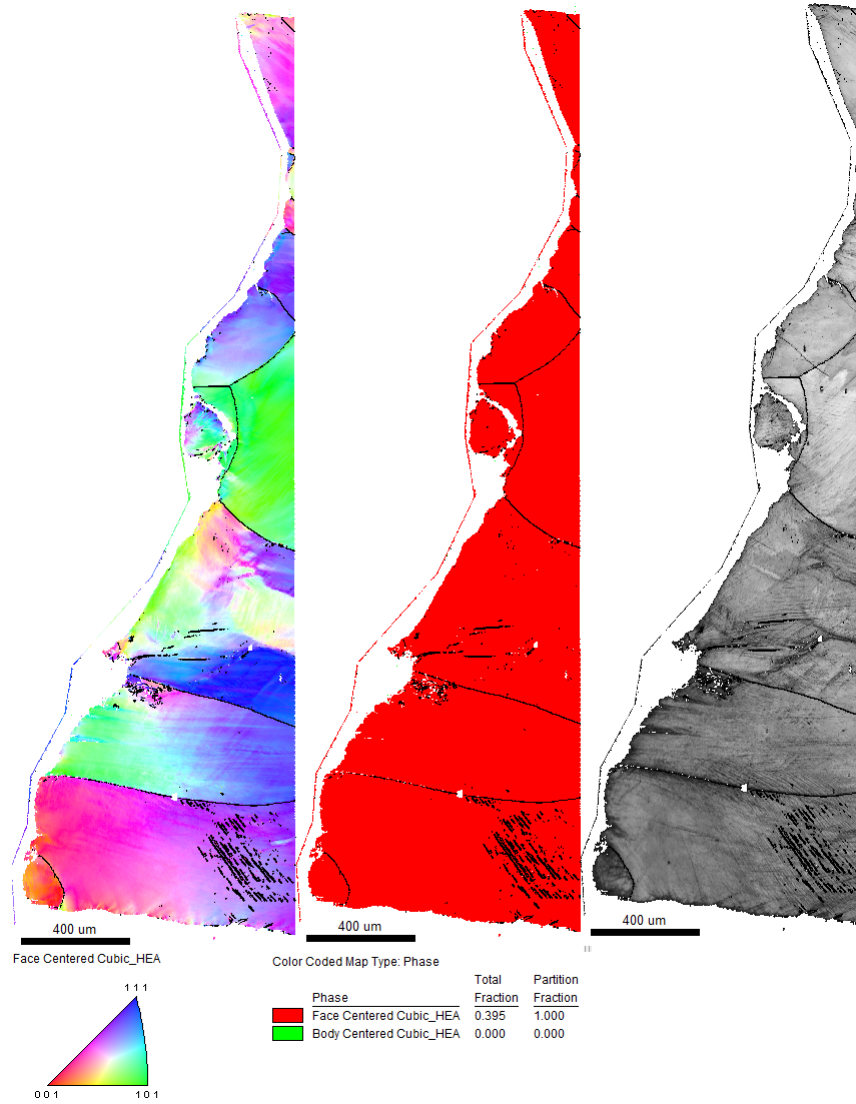


Figure 30: a)inverse pole figure b) phase map c)IQ map

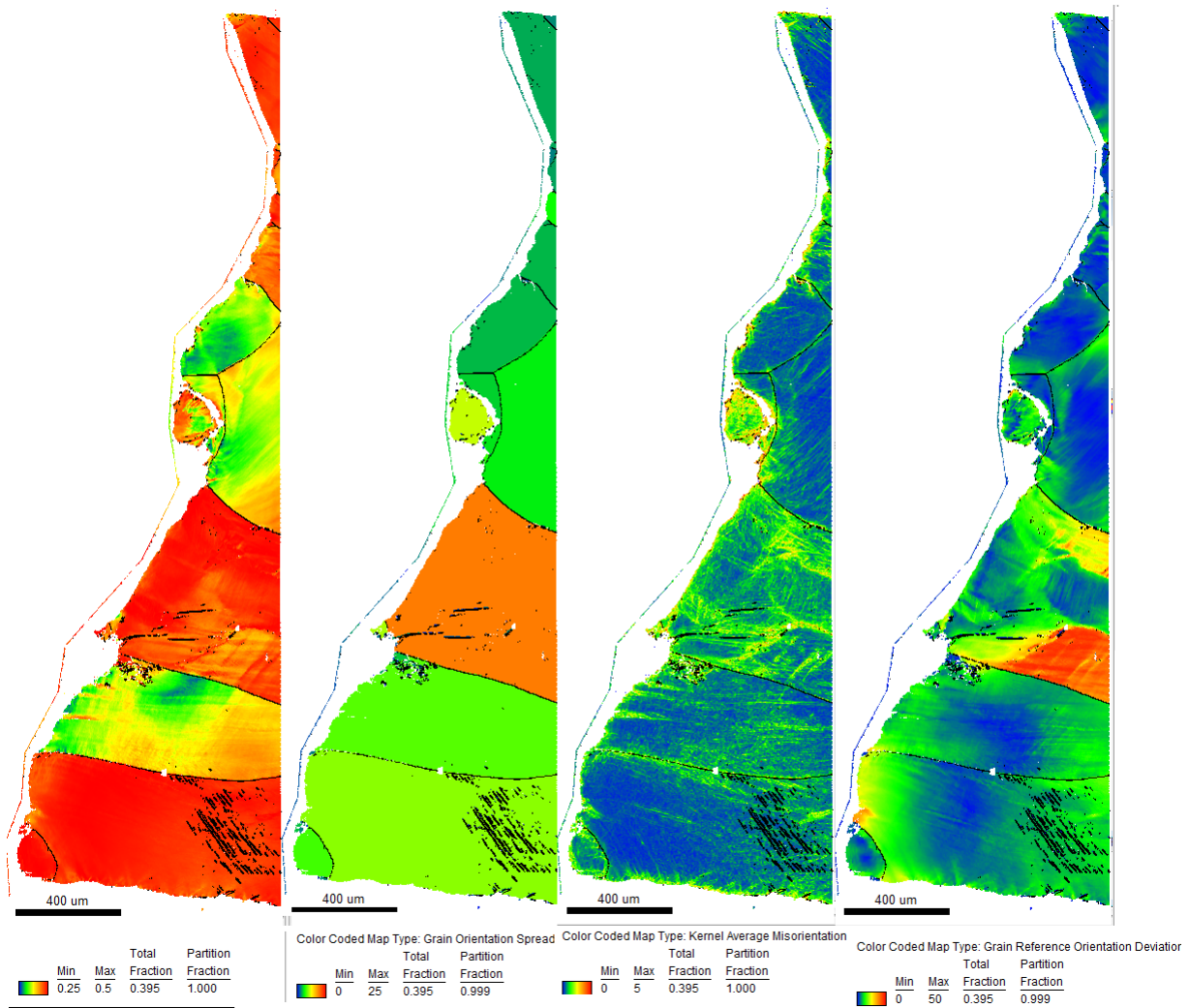


Figure 31: a)Schmidt factor map b) grain orientation deviation c) Kernel average misorientation d) grain reference orientation deviation

5.2.9 Effects observed throughout all samples

The phase diagrams show that after the cleaning process, BCC phases can be disregarded in all samples. It is also observed that IQ maps have a lower image quality near fracture areas (see figure 30(c), 28(c) and 26(c)). On the other hand, fracture areas which did not experience extensive deformation throughout cyclic loading such as figure 24(c) have a more balanced IQ spectrum at the fracture boundary. The inverse pole figure maps present the various crystallographic directions pointing in the z-direction (into the page). Not much can be said with regards to these diagrams independently as their information only becomes

valuable in combination with other diagrams which will be discussed next. An interesting notice is that crystallographic deformation misorientations within a single grain often occur near fracture areas, as expected from theory(see figure 30(a),28(a))

There are also some areas where the microscopy tool was not able to index data points, the result which these points remain blank and cannot be used for data analysis. This effect is observed most intensely in figure 20, 21 and may be the result of an unknown dirt condition to the sample surface or a technical issue with the microscope at that time.

Schmidt factor

From Schmidt's law it is known that a critically resolved shear stress must be attained on an arbitrarily orientated grain in the polycrystal for dislocation motion to occur on one of the slip planes. For the FCC materials investigated, 12 different slip systems are available, the result of which under applied tension, dislocation motion in a single more favourable slip systems(high resolved shear stress) is probable. This trend is observed from most Schmidt factor maps as most individual grains have a Schmidt factor(in the region of 0.4-0.5).

It is also observed that there are gradients in the Schmidt factor, specially close to fracture areas(see Figure 29 (a) for example). Since the Schmidt factor, is defined as:

$$n = \frac{\sigma_{CRSS}}{\sigma} \quad (3)$$

It is recognised that some areas within this grain are more resistant to dislocation motion than others(a low Schmid factor implying easier dislocation motions). This effect is the result of deformation of the grain itself where the grain is deforming in an attempt to align with the stressed axis. This trend can also be confirmed from other IPF diagrams(see 26(a) for an example) where within a single grain a crystallographic direction change is observed which also leads to a gradient change of the schmidd factor.

There are also some planes present which appear to be more resistant to dislocation motion as a whole. Making statements regarding such effect may seem simple from a scientific stand point however, remains a matter of statistics in the observed data. It can be observed from figures 22(a) and the corresponding Schmidt factor, 23(a) that green as well as blue regions on IPF maps(planes between (111) and (101)) have a lower Scmidt factor, and are thus more prone to dislocation motions during cyclic loading. This trend is generally observed throughout all data sets but cannot be used to provide substantial statements regarding the physics of the materials.

5.2.10 Fractured vs non-fractured

Grain reference orientation deviations-strain

The GROD from fractured and non fractured data samples show extensive differences in their magnitude. This effect was so extreme, that a different scale had to be used such that the GROD map from non-fractured and fractured samples still carried information with regards to the localisation of strain distri-

bution inside the grains. The selected factor difference was 5, such that GROD maps from fractured samples have a scale from $0 - 50^\circ$ while non-fractured samples a scale from $0 - 10^\circ$

Regardless of their difference scales, it can be stated that the samples show a fairly similar range in terms of the colours which are presented in the map itself. This implies that fractured samples have internal misorientation distributions which is approximately 5 times smaller than fractured misorientation distributions with respect to the average orientation. Since this is a measure of internal strain we can conclude that fractured samples have approximately 5 times more intensive internal strain distributions .

The localisation of GROD strain distributions is found mostly around at either grain boundaries, or in regions of the grain where IPF diagrams present a change in crystallographic directions(deformation of the grain). This effect is clearly visible in figure 27(d) and 26(a) amongst others and agrees with expectations. Other high GROD distributions may be found in scratched areas, however, these areas are considered as erroneous data and are thus excluded from discussion.

Grain orientation spread

The grain orientation spread presents the average GROD value over a grain. This is in direct agreement with the quantity and intensity of the grains observed in GROD maps. Since the maps are directly related, it was a necessary to pick up a different scale once more. Non-fractured samples have a scale from $0 - 5.1$ and fractured samples have a scale from $0 - 25$. Thus an identical conclusion is drawn as that of the GROD diagrams: fractured sample data points have a much higher misorientation to the grain average when compared to non-fractured samples.

kernel average misorientation

The Kernel average misorientation presents the internal strain as measured within the selected kernel(second neighbours). This yields a rather different type of strain distribution as compared to the previous GROD,GOS diagrams which calculated misorientations with respect to the entire grain. Here strain is locally observed in the Kernel itself, and the distributions present high concentrations near grain boundaries. This would suggest the presence of dislocations piling up at the most favourable point(least energy) where the grain boundary itself is of course excluded since the KAM map method itself is limited to a deviations of 5° .

The sample edges are also frequently points of high KAM values. This seems to be most likely due to the manufacturing conditions of the sample.

Scratches are also very prevalent in KAM diagrams however, similar to GOS diagrams, they are excluded from discussion.

5.2.11 Temperature treatments

To be able to quantify temperature dependent differences, the samples to be analysed are to have been subjected to identical weight as well as mechanical conditions(fractured or non-fractured) with the only difference being the temperature treatment. This situation is encountered in 2 sample groups:

1. fractured, as cast 3114 N and fractured, 400h at 700°C, 3114 N
2. fractured, as cast 3336 N and fractured, 400h at 700°C 3336 N

It is observed that both groups have undergone a different number of cycles up to the crack initiation point due to the heat treatment. In the first group (figure 25(b),(d) (as cast) and 27(b),(d)(heat treated)) it is observed that the heat treated samples, generally have higher KAM and GOS values. Very similar results are observed for the second sample group (Figure 29(b),(d) (as cast) and 31(b),(d)(heat treated)) Thus it can be concluded that:

1. The heat treated samples have undergone approximately 2 times as many fatigue cycles before fracturing when compared to the non-heat treated samples.
2. internal strain distributions regardless of which type of map is used for the analysis, is much higher for heat treated samples.

5.2.12 Cyclic load applied

The most readily available statement regarding the applied load can be easily derived by excluding all heat treated samples. This leaves 3 data sets for analysis. For consistency, only the effects on fatigue affected areas are discussed, since not all non-fatigue affected areas have been analysed.

When, all such images are presented next to one another, it is observed that an increase in the applied load leads to an increase in the GOS as well as KAM values as expected. Thus it can be simply concluded, that the sample deformation/internal strain is proportional to the magnitude of the subjected weight load. The difference in magnitude of both scales are taken into account in order to derive the resulting statement.

5.3 Discussion

It must be mentioned that most of the results derived in this subsection are explained purely on the basis of visual differences and highlights observed throughout all maps used, making the concluded statements vulnerable to debate.

For starters, it is observed that that IPF maps do not clearly allow one to derive which crystallographic directions have a higher Schmid factor since various maps contain data which deviates from the mentioned result. The resulting statements made regarding such samples found were purely made due to their known theoretical relation to crystal plasticity of perfect crystals.

It is also observed that the internal strain magnitude difference between fractured and non-fractured samples(factor ≈ 5), was also made based on what was generally observed regardless of the fact that some maps may disagree with this factor difference. Similar statements can be made regarding the grain orientation spread.

KAM maps did have some agreement to an extent with the theory regarding the presentation of the fact that dislocation distributions pile up close to grain

boundaries in the forms of persistent slip bands. On the other hand, there were also large strain distributions present which were not anywhere close to the grain boundaries. This might suggest that there are various more points of minimum energy throughout a single grain for dislocations to pile up on. Temperature treatment analysis allowed for a more careful analysis by locking out two groups of samples. Both groups show similar microstructural effects due to the heat treatments however, it must be acknowledged that only two sample groups were studied, which again brings about the fact that the conclusions drawn are merely statistical.

6 Conclusion

In this research, EBSD was used in order to scan large areas (several *mm*) of $Al_{0.1}CoCrFeNi$ high entropy alloys in order to analyse their mechanical characteristics.

The scanning of large areas posed a problem for EBSD technology due to the limited step size of the A/D converter which directs the electron beam in a single scan field. Because of this limitation, it was proposed that single large scans not be taken and that instead, various high magnification small scans be made which could subsequently be merged together using advanced software tools. This method would have helped in overcoming the limitations to the step size in the scanning field, however produced various distorted data maps which could not be merged together for an accurate analysis since the size and length of various microstructural features did not match together.

This resulted in further research regarding the different distortion effects present and their magnitude at different magnifications.

Two key distortion effects were found both of which were inversely proportional to the selected magnification and were quantified for the specific microscope in use:

1. the trapezoidal distortion, whose magnification drops below 0.5% at magnifications of ≈ 2000
2. the fish-eye distortion, whose magnification becomes immeasurable at magnification above ≈ 500 .

On top of these distortions it is also realised that SEM images carry an intrinsic vertical distortion, the result of which the right hand side of the image captured is more elongated than the left hand side. This distortion is directly translated into EBSD maps, causing the distance between EBSD measured map points to not be constant but to depend on the SEM image distortion.

Since, various issues were encountered with merging of high magnification scans it was decided to use low magnification scans which although suffered from weaknesses already mentioned (minimal step size in scan field due to A/D converter), could provide for an accurate analysis regarding the microstructure of

the high entropy alloys analysed.

This method proved successful in the determination of microstructural characteristics regarding the alloys and allowed for general conclusions to be drawn regarding the effects of heat treatments, different number of loading cycles/forces and key differences between fractured and non-fractured samples.

For any reader interested in the scanning of large areas using similar EBSD technology, the following approaches are advised:

1. merging of data sets: If this method is selected, the user must be aware that vertical merging of same sized data maps can be done without issues, however the merging of horizontal scans will become a problem due to the distortions presented in this report. In order to overcome the distortions, it is advised to use very high magnification scans, such that the effects are minimised and do not influence results. According to the results proposed in this paper, this can be done for a single scan without too much trouble, but if attempted with various batches of vertically merged scans, it will result in the superposition of the distortion effects leading to unaligned data maps.
2. Large scans: This method will be easier to perform and more time effective. As mentioned before the method is limited by the precision of A/D converters on a single scan field, but will not produce unaligned data maps since merging is not involved.

Finally, it is recommended that all users of EBSD as well as SEM technology regardless of which scan type is performed and which system type is used be aware of the distortions present while using SEM which directly translate into EBSD results, regardless of the fact that they may not appear present in data maps.

7 Appendices

tilted XHD scan:	X_L	X_R	X_B	X_T	
50x	137,79	124,46	521,56	542,58	
100x	277,58	251,58	1044,99	1085,71	
200x	540,84	515,93	1044,56	1084,32	
500x	909,10	889,37	1191,65	1223,37	
1000x	940,65	929,84	1268,50	1286,47	
3000x	904,46	901,48	1208,56	1213,77	
tilted XHD scan:	vertical distortion	horizontal distortion	vertical error	horizontal error	
50x	9,67		3,87	2,06	0,52
100x	9,37		3,75	1,02	0,26
200x	4,61		3,67	0,52	0,26
500x	2,17		2,59	0,31	0,23
1000x	1,15		1,40	0,60	0,44
3000x	0,33		0,43	0,63	0,47

Table 2: table presenting the various distortions at different magnifications taken with SEM software. All measured parameters are consistent with those presented in 7.

tilted DC scan):	X_L	X_R	X_B	X_T	
50x	146,42	132,06	560,56	582,05	
100x	291,11	270,36	840,46	871,76	
200x	573,96	552,27	840,01	870,15	
500x	907,82	894,37	855,54	875,87	
1000x	943,79	936,44	932,13	942,04	
3000x	928,49	926,46	905,61	910,14	
tilted DC scan):	vertical distortion	horizontal distortion	vertical error	horizontal error	
50x	9,81		3,69	1,94	0,49
100x	7,13		3,59	0,97	1,02
200x	3,78		3,46	0,49	0,98
500x	1,48		2,32	0,31	0,65
1000x	0,78		1,05	0,60	0,55
3000x	0,22		0,50	0,61	0,27

Table 3: table presenting the various distortions at different magnifications taken with EBSD software. All measured parameters are consistent with those presented in the theory

	non-tilted XHD	L'_M	L'_u	L_M	L_R	
	50x	581,5	576,43	584,46	579,09	
	100x	1161,25	1163,45	899,06	896,36	
	200x	1069,7	1070,65	809,05	807,82	
	500x	1208,41	1207,89	811,92	811,13	
	1000x	1208,75	1209,44	881,44	881,51	
	3000x	1088,35	1089,02	855,47	855,69	
	non-tilted XHD	horizontal distortion	vertical distortions	horizontal error	vertical error	
	50x	0,78	0,92	0,49	0,48	
	100x	0,58	0,30	0,24	0,31	
	200x	0,21	0,15	0,26	0,35	
	500x	0,12	0,10	0,23	0,35	
	1000x	-0,06	-0,01	-0,47	-0,64	
	3000x	-0,09	-0,03	-0,52	-0,66	

Table 5: measurements of the fish eye effect as taken with SEM software. All parameters presented are consistent with figure 8. Do not that two other variables are present: L'_m and L'_u which are not in figure 8. These variables present identical measures to both L_m and L_R but are turned 90° such that they present the horizontal lengths.

8 References

References

- [1] Michael D.Sangid. *The physics of fatigue crack initiation*. URL: <https://www.sciencedirect.com/science/article/pii/S0142112312002940>.
- [2] EDAX. *EBSD pattern indexing*. URL: <https://unishare.nl/index.php/s/2FA4Q8FasUUrhzJ#pdfviewer>.
- [3] EDAX. *TSL OIM analysis 8*. URL: [TSL%20IM%20analysis%20help%20sections](https://www.edax.com/Products/200IM%20analysis%20help%20sections).
- [4] Max-Planck-Institut für Eisenforschung. *Electron backscatter diffraction - EBSD*. URL: <https://www.mpie.de/3077954/EBSD>.
- [5] E.J.Pickering N.G. Jones. *High-entropy alloys: a critical assessment of their founding principles and future prospects*. URL: <https://www.tandfonline.com/doi/abs/10.1080/09506608.2016.1180020>.
- [6] Gert Nolze. *image distortions in SEM and their influences on EBSD measurements*. URL: https://www.researchgate.net/publication/6780070_Image_distortions_in_SEM_and_their_influences_on_EBSD_measurements.
- [7] D.B. Miracle O.N. Senkov. *A critical review of high entropy alloys and related concepts*. URL: <https://www.sciencedirect.com/science/article/pii/S1359645416306759>.

- [8] V.Randle. *microstructure determination and its applications Second Edition. The institute of materials, minerals and mining.* URL: <https://unishare.nl/index.php/s/7fda4b3ded842abac5cb78fbb6638252#pdfviewer>.